

UNIVERSITY OF GENEVA

MASTER THESIS

---

**Thin Time-of-Flight PET scanner: expected performance  
analysis and image reconstruction.**

---

*Author:*

Daniele VITTURINI

*Supervisor:*

Prof. Giuseppe IACOBUCCI

Dr. Emanuele RIPICCINI

*A thesis submitted in fulfillment of the requirements  
for the Master's degree in Physics*

*in the*

TT-PET Group

Department of Nuclear and Subnuclear Physics

September 15, 2019



# Contents

<b>1</b>	<b>Introduction</b>	<b>1</b>
1.1	Organization of the manuscript . . . . .	3
<b>2</b>	<b>Positron Emission Tomography</b>	<b>5</b>
2.1	Positron Emission . . . . .	6
2.2	Basics Concepts about PET reconstruction . . . . .	7
2.3	Time-of-Flight PET . . . . .	9
<b>3</b>	<b>TT-PET Scanner</b>	<b>13</b>
3.1	Scanner Layout . . . . .	13
3.2	Detection layer . . . . .	16
3.2.1	The Monolithic Pixel Sensor . . . . .	17
3.3	Read-out System . . . . .	18
<b>4</b>	<b>TT-PET Scanner: Expected Performance</b>	<b>21</b>
4.1	Scanner simulation . . . . .	22
4.2	Type of Coincidences . . . . .	23
4.2.1	True, Random and Scattered Coincidences . . . . .	23
4.2.2	Noise Equivalent Count Rate . . . . .	25
4.3	Time Coincidence Window . . . . .	26
4.4	Coincidence rate . . . . .	27
4.4.1	Read-out system effect on data rate . . . . .	33
4.5	Scanner Sensitivity . . . . .	33
4.6	Expected spatial resolution . . . . .	34

<b>5</b>	<b>Image Reconstruction</b>	<b>37</b>
5.1	Derenzo phantom image reconstruction . . . . .	38
5.1.1	Reconstruction with filtered back projection . . . . .	38
5.1.2	Image Reconstruction with Penalized ML-EM Algorithm	40
<b>6</b>	<b>Conclusions</b>	<b>45</b>
	Scanner simulation . . . . .	45
	Image Reconstruction . . . . .	47
<b>A</b>	<b>Image Reconstruction Techniques</b>	<b>49</b>
A.1	Filtered Backprojection . . . . .	52
A.2	3D Reconstruction . . . . .	54
<b>B</b>	<b>Iterative Reconstruction Algorithms</b>	<b>55</b>
B.0.1	Expectation-Maximization Algorithm . . . . .	57
	<b>Bibliography</b>	<b>59</b>

# Chapter 1

## Introduction

Cancer is one of the leading causes of death worldwide and the number of new cases is on the rise globally [1]. Diagnosing, staging, and follow-up of various malignancies, as well as the planning and monitoring of cancer treatment, have commonly been linked to anatomic imaging with magnetic resonance imaging (MRI) or computed tomography (CT). These anatomic imaging modalities provide essential details that are useful for guiding surgical intervention and radiotherapy. On the other hand, they have limitations in their ability to characterize tissue reliably as malignant or benign and cannot demonstrate abnormal metabolic activity in organs that as yet do not show an abnormal appearance based on morphologic criteria [2]. That is why, to accurately discriminate benign from malignant tissues, the nuclear medicine community has developed positron emission tomography (PET). The aim of the TT-PET project (Thin Time-of-Flight PET) is to develop a PET scanner with a very high time resolution. Enhancing the time resolution of a typical PET scanner allows to determine with higher precision the position of the malignant tissue. With PET we measure the activity of an injected radionuclide similar to glucose, such as the Fluorine-18-deoxyglucose (FDG). This technique is based on the fact that malignant tissue typically exhibits significant increased rates of glucose metabolism. FDG, having a similar behaviour to glucose, is actively transported into cells mediated by a group of structurally related glucose transport proteins so that we can find tumour cells on

the basis of the number of glucose transporters ([2], [3]). In this way, PET provides imaging of the whole body distribution of FDG, thus highlighting the markedly increased metabolic activity of tumour cells. A whole-body FDG PET scan of a patient with cancer is shown in Figure 1, where the dark spots represent widespread metastatic.



FIGURE 1.1: A whole-body  $^{18}\text{F}$ -fluorodeoxyglucose PET scan (injected activity 370MBq) of a patient with cancer, showing widespread metastatic disease (dark spots). The scan took 14 minutes to acquire (7 overlapping bed positions to cover thorax and abdomen, 2 minutes per bed position), with imaging commencing 60 minutes post-injection [4].

The FDG is not absorbed only by cancer cells but can accumulate in any areas of high rates of metabolism and glycolysis. Therefore, increased uptake can be expected in all sites of hyperactivity at the time of FDG administration, at sites of active inflammation, and at sites of active tissue repair. FDG

also is used diagnostically in conjunction with blood flow tracers to evaluate cardiovascular disease (myocardial viability, coronary artery disease). In the brain, PET is used diagnostically in a range of neurodegenerative diseases (Alzheimer's disease, Parkinson's disease) and dementia, for epilepsy, neurodevelopmental disorders and in psychiatric disorders [4]. Many other PET radiotracers are used for research studies and are being developed for future clinical use. They are first evaluated in animal models using a dedicated animal PET scanner. The experience gained with the construction of the detectors at the CERN Large LHC Hadron Collider has been transferred into medical physics applications, PET is one of them. In the TT-PET project, thin semiconductor detectors in combination with a very fast reading electronics and very low background noise, developed for the LHC ATLAS experiment [5], are proposed for the realization of the PET system with high precision and will be shown in this thesis.

## 1.1 Organization of the manuscript

This manuscript is composed of 5 parts. In the next chapter we will present a general overview on the PET techniques and benefits for the human healthcare. Chapter 3 is dedicated to the description of the TT-PET scanner and the construction of the detector, giving the main physical characterisations. In Chapter 4 the performance analysis of the detector will be presented. Chapter 5 will focus on image reconstruction. Finally in Chapter 6 I will summarize the results achieved with the thesis.





## Chapter 2

# Positron Emission Tomography

Positron emission tomography (PET) is based on the detection of back-to-back  $\gamma$  rays coming from the annihilation of a radio-emitted positron with an electron of the surrounding matter. Small amounts of radioactive materials, called radiotracers, are used to map the metabolic activity of the body. A radiotracer is composed by the carrier and the radionuclide. The first one is a molecule with the biological function of transporting the radionuclide to the zone of interest. The second one is an unstable atom that allows the tracking of the radionuclide in the body, through the use of appropriate instrumentation.

PET is one of the major techniques for tomographic imaging in modern nuclear medicine. Tomographic images are 2-D representations of the structures that are within a particular plane of a 3-D object. Modern Computed Tomography (CT) techniques, including PET, use detector systems placed around the object in order to obtain many different angular views (projections) of the object. From these projection data it is then possible to reconstruct images of selected planes within the object of interest using mathematical algorithms. The process of reconstructing the images from multiple projections obtained by detecting the emissions from radionuclides within the body is known as emission computed tomography (ECT).

## 2.1 Positron Emission

In radioactive decay by positron emission we indicate the process in which, a proton ( $p$ ) in the nucleus is transformed into a neutron ( $n$ ) with the emission of a positron ( $e^+$ ) and an electronic neutrino ( $\nu_e$ ). The positively charged electron—or positron ( $\beta^+$ )—and the neutrino are ejected from the nucleus. Schematically, the process is:



The PET tomography uses positron emitting radionuclides in order to obtain the production of the back-to-back  $\gamma$  rays. After the source decay the emitted positron loses its kinetic energy interacting with the surrounding matter until it comes to rest, usually within a few millimetres from the decay site. Near the end of its path the positron annihilates with an electron and in this process are produced two back-to-back  $\gamma$  rays that have identical energies,  $0,511\text{MeV}$  if annihilations is at rest.

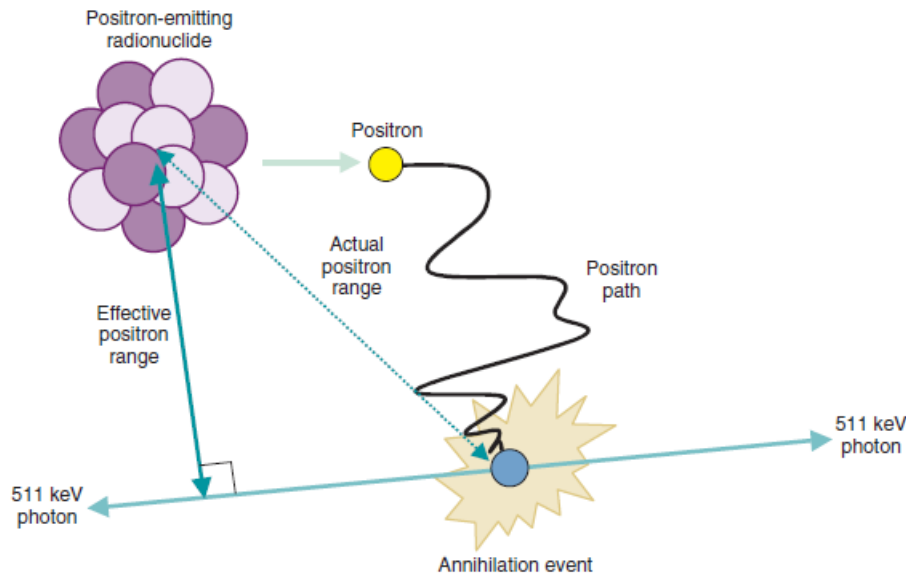


FIGURE 2.1:  $\beta^+$  decay mechanism that lead to the production of the two  $\gamma$  rays detected by the PET.

The detection of the two prompt  $\gamma$  rays in the PET scanner allows the

localisation of a line between the two detectors (line of response) in which the two rays have been produced. This mechanism is known as *annihilation coincidence detection* (ACD). Due to the granularity of the detector the line of response is not a simple line, instead what is defined is the volume from which they are emitted.

Coincidence logic is used to analyse the signals from opposing detectors. A coincidence event is assumed to occur when two events, with given characteristics, are recorded within a specific coincidence timing window. The timing window is necessary to take into account the different distances traveled by  $\gamma$  rays before being detected as well as the finite timing resolution of the PET scanner.

## 2.2 Basics Concepts about PET reconstruction

With the aim to have a simpler approach to the basic concepts used in PET imaging a one-dimensional configuration shown in Figure 2.2 has been used. In this case data are collected with a detector, a gamma camera, fitted with a parallel-hole collimator. While using this configuration provides a good example for explaining many PET features, it is important to point out that the configuration is different from the one used in TT-PET project. The collimated detector is assumed to accept radiation only from a thin slice direct perpendicular to the face of the detector. This slice defines the *line of response* for the collimator hole.

The sum of the counts recorded for each collimator hole measures the activity along the line of response. This quantity is called *line integral* for the line of response and a full set of line integrals is called *projection profile*. Detectors acquire a set of  $N$  projections at equally spaced intervals around the object of interest, then the 2-D distribution of activity is reconstructed using mathematical algorithms.

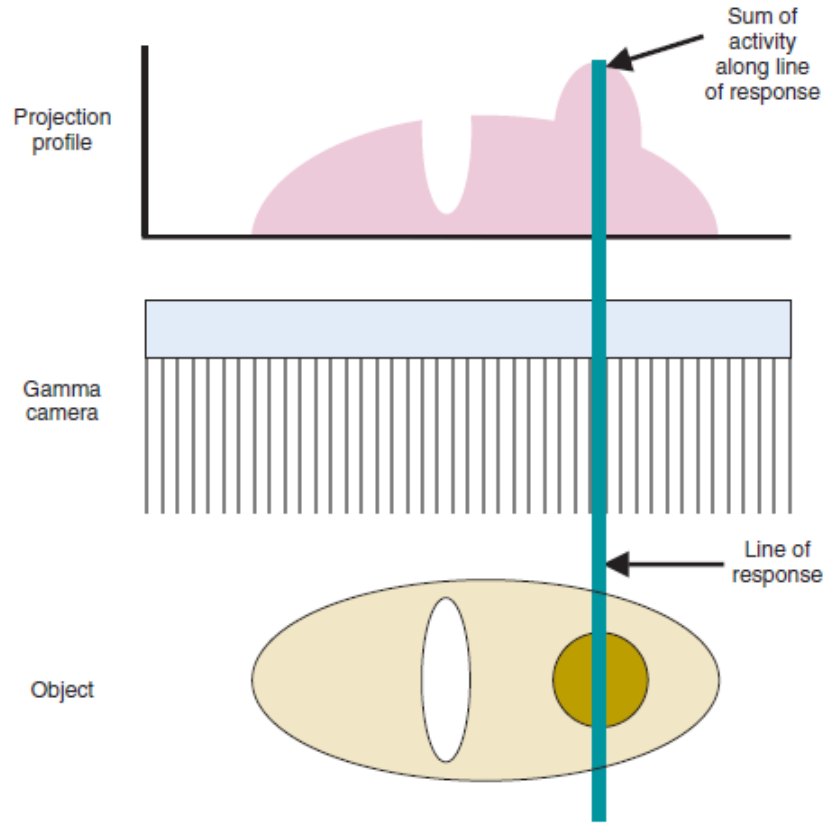


FIGURE 2.2: Cross-section of the response characteristics of an idealized gamma camera. Image taken from [4].

One of the most important steps in the image reconstruction algorithm process is building the *sinogram*. A sinogram is based on line integral and Radon transform. When considering an object represented by a two dimensional function  $f(x, y)$  it is convenient to introduce a new coordinate system,  $(r, s)$ , that is stationary with respect to the detector. If the detector is rotated by an angle  $\phi$  with respect to the  $(x, y)$  coordinate system of the scanned object, the equations for passing from a coordinate system to the other are:

$$r = x \cos \phi + y \sin \phi \quad (2.2)$$

$$s = y \cos \phi - x \sin \phi \quad (2.3)$$

In this way we obtain an object represented by a two dimensional function  $f(x, y)$  and each line integral by  $(\phi, r)$  parameters. Using equation 2.2

and the delta function is now possible to express the relationship of line integral  $P\phi(r)$  as:

$$P\phi(r) = \int_{-\infty}^{\infty} \int_{-\infty}^{\infty} f(x, y) \delta(x \cos \phi + y \sin \phi - r) dx dy \quad (2.4)$$

The function  $P\phi(r)$  is known as the Radon transform of the function  $f(x, y)$ . A projection is then formed by combining a set of line integrals. The full set of projection data is displayed as a 2-D matrix  $p(r, \phi)$ , the representation of this matrix is called a *sinogram*, Figure 2.3.

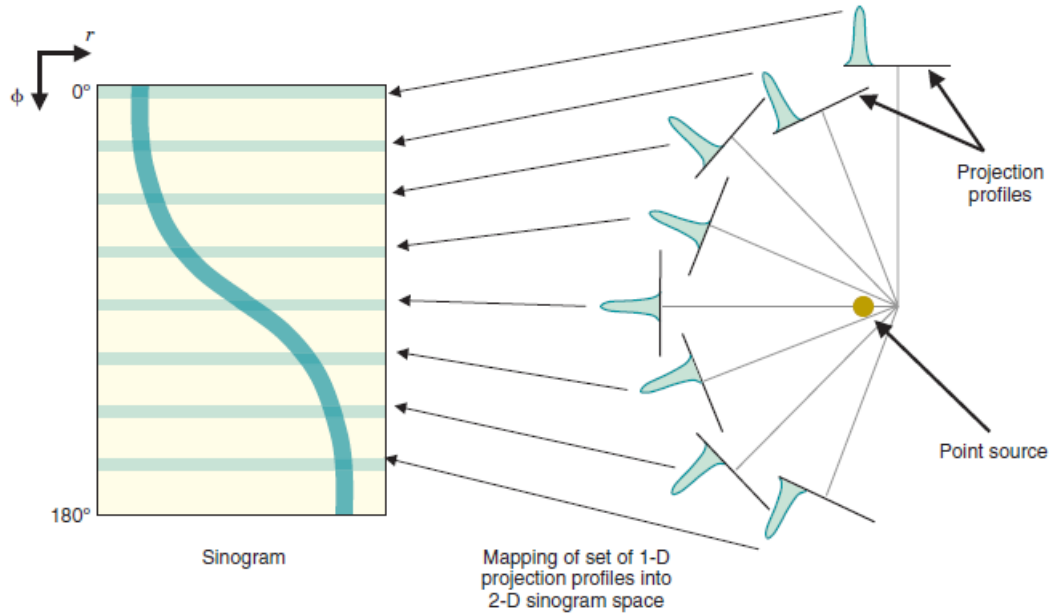


FIGURE 2.3: A set of 1-D projection profiles mapped in a 2-D sinogram. Image taken from [4].

## 2.3 Time-of-Flight PET

These type of PET scanners use the information about the time at which the coincidence  $\gamma$  rays are detected by the scanner to determine the location where the annihilation occurred along the line between the two detectors.

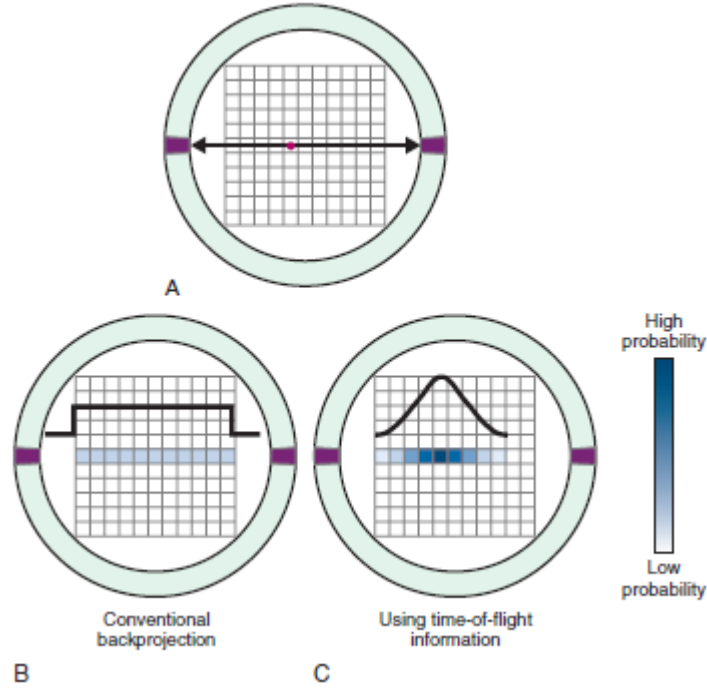


FIGURE 2.4: The addition of time-of-flight information constrains the back-projection of data along one particular line to a smaller region of the reconstructed image matrix.

Given the arrival times of the two  $\gamma$  rays and their difference,  $\Delta t$ , the location of the annihilation event, with respect to the midpoint between the two detectors is:

$$\Delta d = \frac{\Delta t \times c}{2} \quad (2.5)$$

We can find the expected TOF resolution from the full width at half maximum (FWHM) of the distribution of the time difference between the times of arrival of the two coincidence  $\gamma$  rays. The TT-PET project aims to obtain a time resolution of  $30ps$ . According to equation 2.5 reaching the project's goal for the time resolution would mean to achieve a depth resolution of less than half a centimeter. The convenience of using TOF detectors is shown in Figure 2.4. We consider the case of a pair of  $\gamma$  rays emitted by a source and detected in coincidence by opposing detectors, A. In B is shown the conventional back-projection case, where no time information is known. The probability distribution is uniform and the particles could have been originated

in any of the pixels in the line of response. When time-of-flight information is added,  $C$ , the probability distribution follows a Gaussian centered on the pixel that has the highest probability of being the one in which the annihilation occurred. The timing resolution of the detector gives us the FWHM of the distribution.

It is possible to see how the TOF technique helps in finding the true origin of the annihilation by comparing the results obtained by a PET detector that does not have a TOF reading system and another one with TOF information. In Figures 2.5 and 2.6 a traditional PET is shown. For each pair of  $\gamma$  rays is associated a line of response. The points where the lines cross each other are candidate emission points. It is evident that reducing the lines of response to segments reduces the noise and thus is easier to locate the radiation source.

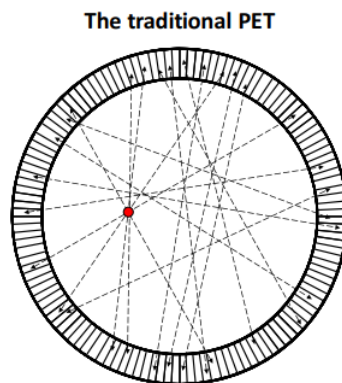


FIGURE 2.5: Some line of responses obtained by a PET detector without ToF.

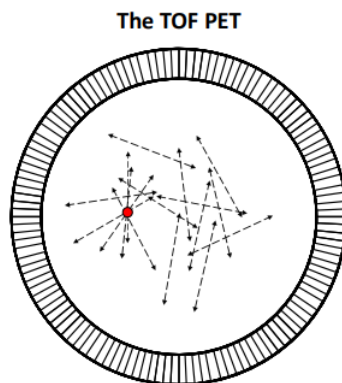


FIGURE 2.6: Adding time of flying information reduces significantly the number of fake coincidences.





## Chapter 3

# TT-PET Scanner

The aim of the TT-PET (Thin TOF-PET) project is to develop a novel compact TOF-PET scanner for small animals, based on fast silicon detector featuring 30 ps time resolution, intended to be inserted in an existing commercial MRI scanner. This value is well beyond the state-of-the-art for time-of-flight PET systems [6], and is obtained with a radically different approach compared to traditional scanners.

The TT-PET project started on March 2016 involving the department the physique nucléaire et corpusculaire (DPNC) of the University of Geneva, the Geneva Cantonal Hospital, HUG, and the Laboratory for High-Energy Physics (LHEP) of the University of Bern and is developed in collaboration with CERN, the Department of Physics of the University of Rome Tor Vergata, the INFN and IHP Microelectronics.

### 3.1 Scanner Layout

The scanner and its supporting mechanics are designed to be placed inside the removable RF-coil of the nanoScan 3T MRI machine [7]. While all the readout electronics and power supplies will be located outside of the MRI machine, and connected using long flat shielded kapton cables. This configuration is done to remove sensitive electronics from the magnetic fields inside the MRI machine, making shielding and cooling simpler. The design of the

TT-PET scanner is shown in Figure 3.1, the scanner is divided in 16 tower modules and 16 cooling blocks arranged in an alternating pattern. Each tower module is composed by a stack of layers of high-Z photon-converter and 100  $\mu\text{m}$  thick silicon sensors, the result is a scanner with  $0.5 \times 0.5 \times 0.2\text{mm}^3$  granularity with precise depth-of-interaction measurement. The main feature of the detector is to combine high granularity to a fast time response. The high time resolution is achieved by using thin silicon layers.

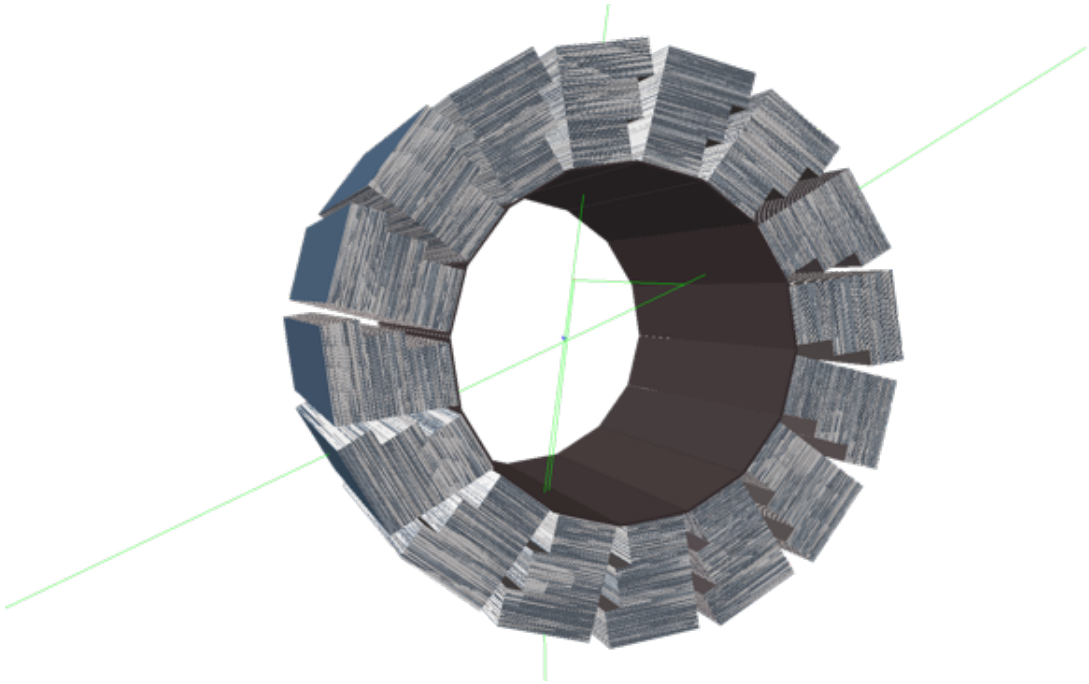


FIGURE 3.1: Scanner overview

The scanner has a total length of 4.8 cm, an internal radius of 1.8 cm and an external radius of 4.2 cm. The active part of the detector ring is made of the 16 wedge-shaped units called towers (Figure 3.1) and each one of these towers is composed by:

- 60 detection layers of three different sensor widths (7,9,11 mm).
- Each detection layer is made of 50  $\mu\text{m}$  thick converter layer, a 55  $\mu\text{m}$  thick flex layer (for signal transmission and sensor control) and a 100  $\mu\text{m}$  thick silicon layer (Figure 3.2)

- Each silicon layer is formed by two 2.5 cm long chips like shown in (Figure 3.5). The active area of the chip is segmented in detection pads of  $0.5 \times 0.5 \text{ mm}^2$ .

The three chip types differ in the number of pads, the total number of read-out channel in the scanner is 1'474'560. The geometrical acceptance of the scanner has been studied with a Monte Carlo simulation for 511 KeV  $\gamma$ -rays produced in a point at the center of the scanner and isotropically emitted. The resultant geometrical acceptance is 78% [8].

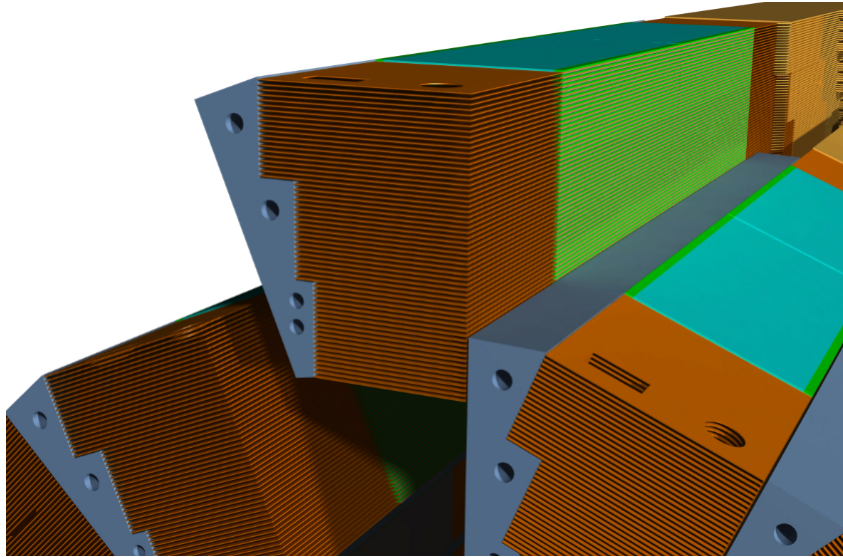


FIGURE 3.2: View of one of the cells of the detector.

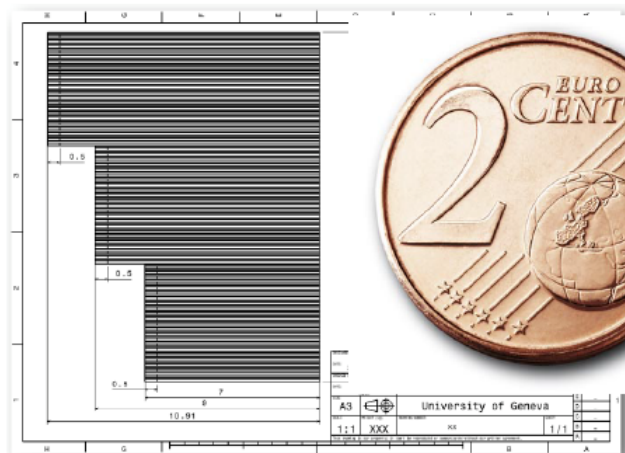


FIGURE 3.3: Cell dimension compared to 2 cents coin.

Every tower module is separated from the next one by a cooling block in order to maintain constant the temperature of the detector. The silicon sensor system generates around  $20 \text{ mW/cm}^2$  of heat; to deal with this heat production a cooling plate has been implemented in the inner-cell gap. The plate is made by 3D-printed *Al – nitride*, this material has been chosen for its relatively high thermal conductivity ( $20 \text{ Wm}^{-1}\text{k}^{-1}$ ) and for the possibility of operating inside an MRI. The result is a very stable and homogeneous overall detector temperature, with expected stability at the order of  $0.1^\circ\text{C}$ . This is crucial because the detector temperature is directly linked to its performance.

## 3.2 Detection layer

The basic detection element is the module in Figure 3.2. Each module is made of a  $50 \mu\text{m}$  lead layer, which is the converter of the photons in electrons. The thickness of this layer was kept as low as possible in order to have a good ratio between the probability from the photons to be converted by the lead and the probability of the outgoing electron to not be absorbed by the lead layer and reach the sensitive part of the module. The necessity of thin lead layer but together with the necessity to have a sufficient stopping power to be able to convert a significant percentage of the incoming photons has led to the developing of the final design of the towers that consists of 60 thin layers stacked together (Figure 3.1). After the lead converter layer a  $50 \mu\text{m}$  dielectric spacer layer was placed in order to keep the sensor capacitance small. Finally there is a  $100 \mu\text{m}$  monolithic silicon layer that is the sensitive part of the layer. The different parts of the single detection element are glued together by a  $5 \mu\text{m}$  double-sided coated tape. The efficiency of a single element for 511 KeV photons is 0.6%. Each layer is made by two chips, bump bounded on a module flex, these modules are then combined five by five in a super-module. Each super-module is connected with his own data flex for data readout.

The whole tower is composed of twelve super-module and has a detection efficiency of 27% for photons of the same energy arriving perpendicularly at the centre.

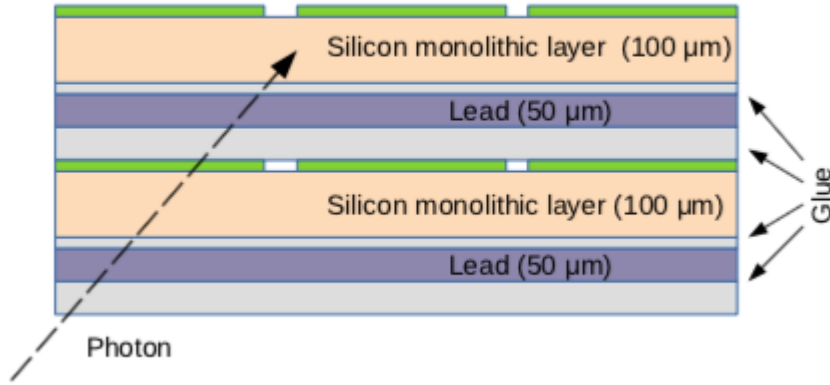


FIGURE 3.4: Representation of two consecutive detection layers

### 3.2.1 The Monolithic Pixel Sensor

The development of the monolithic pixel sensor has been one of the main challenges of the project because, traditionally, silicon pixel detectors focus on accurate position measurement instead of time resolution measurements. The target 30 ps sensitivity for 511 KeV photons represents an improvement of around two orders of magnitude compared to the existing monolithic silicon pixel sensors. Reaching this goal has required to push the limits in the detector design, in the electronics technology and design and to take advantage of the physical properties of the sensor. The time resolution of the detector depends mainly on the performance of the amplifier. To achieve the challenging time resolution required by the TT-PET, the sensor uses a high frequency Si-Ge BiCMOS technology for signal amplification and digitalization. An additional challenge has been to reach these goal with a monolithic structure, so with both sensor and electronics integrated in the same chip. The convenience of having a monolithic sensor with integrated front-end,

time to digital converter (TDC), logic and serializer is that simplifies interconnections, which is a fundamental characteristics for a compact scanner.

The  $500 \times 500 \mu\text{m}^2$  area pixel are organized in matrices of different dimensions, from  $18 \times 46$  to  $26 \times 46$ , depending on the chip size. The pixel size is a compromise between input capacitance, space resolution and power consumption. The small pixel size was selected to reduce noise, by reducing the pixel capacitance, and to remain within the power budget of the scanner, that is set by the cooling system. In addition the quality of the images produced by the scanner would not benefit from smaller pixels since a PET image has an intrinsic resolution of about  $500 \mu\text{m}$  ([9]). A demonstrator chip containing a  $3 \times 10$  pixel matrix, (shown in Figure 3.5) was realized and tested with radioactive sources and in the SPS beam test facility at CERN [10]. The results showed full effective operation for MIP and state of the art time resolution.

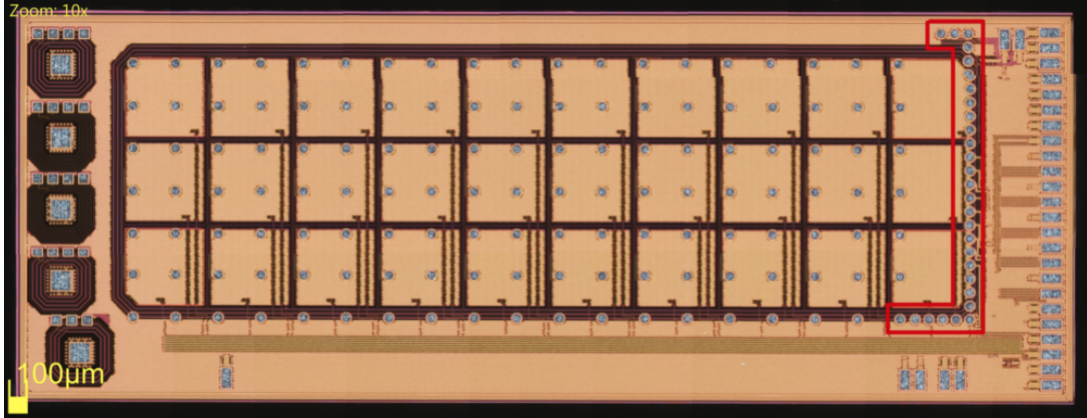


FIGURE 3.5: Layout of the TT-PET demonstrator chip, with a  $3 \times 10$  pixel matrix.

### 3.3 Read-out System

The read-out system is one of the main factors that could influence the counting rate capability of the scanner. In addition it also dictates the capability of the scanner of avoiding saturation and the loss of coincidence events, this will be explained in detail in the next chapter. The read-out system, or data

acquisition (DAQ) system, has been designed to be scalable, that is why it has a modular structure. Since the TT-PET scanner is intended to be placed inside an MRI, the daq system was structured so that the electronic components are kept outside of the bore of the MRI to avoid interference with the magnetic fields. The daq system is divided in three different *stages* [11] as shown in Figure 3.6.

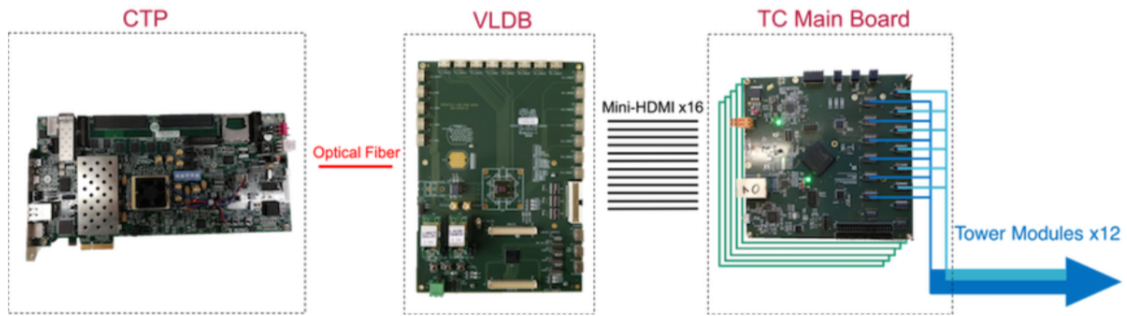


FIGURE 3.6: Overview of full data acquisition chain of the TT-PET scanner, showing from left to right; Central Trigger Processor (CTP), Versatile Link Demo Board (VLDB), and TC Main board.

To reduce the number of flex cables that connect to the scanner the 60 layers of a tower are grouped in 12 super-modules of 5 layers each. From the super-modules the signal is sent, via shielded kapton flex cables, to the Tower Control (TC), which is the first *stage* of the daq system. The Tower Control boards organise the event data and associate them with a clock cycle identifier (ccID) which is sent to the Central Trigger Processor (CTP) for comparison. The CTP is a large powerful commercial FPGA board that is the last *stage* of the daq system and controls the whole daq chain. Here is where coincidence checks are performed and if the ccID values for the recorded events pass the coincidence trigger, the full event data to be sent along the full daq chain to the CTP

The second *stage* of the daq system is a multiplexer board, named, Versatile Link Demo Board (VLDB) which accepts electrical signals from multiple TC boards and multiplexes their output to a single bitstream before being

buffered and converted to an optical signal. The multiplexed data is then sent to the CTP using a single data link and fiber optic cable at a maximum link speed of 4.28 Gbps.



## Chapter 4

# TT-PET Scanner: Expected Performance

The expected performance of the TT-PET scanner has been estimated using a GEANT4 [12] simulation designed following the NEMA procedure [13]. This procedure defines a standardized methodology for evaluating the performance of positron emission tomography (PET) designed for small-animal imaging. The main target of our study is to measure the capability of the detector to accurately select the coincidence events while reducing as much as possible the background noise. We can say that a coincidence event happens when two particles hit the detector within a selected time window. The time window opens when the first particle arrives in the detector, if one or more signals arrive during this period we will have a coincidence, or a multiple coincidence. Selecting the correct time window value is crucial for this analysis because a small value will cause a significant loss of real coincidences while a large value will increase the noise in the measurement generated by random coincidences. The coincidences that we detect are not all of the same type, on the contrary, they depend on several factors like the origin of the  $\gamma$  rays, the path that they have taken before entering the scanner and what happens to them inside the scanner. Different type of coincidence events will be analyzed hereafter. Consequently it is important to define those events in detail before further proceeding with the analysis of the performances of the

scanner.

## 4.1 Scanner simulation

The simulation of the performances of the TT-PET scanner was performed using the GEANT4 software. The simulation provides hit information in terms of position, time and energy deposit in the silicon sensor. A custom software was developed to process the information obtained from the GEANT4 simulation.

In developing this custom software several effects were taken into account. To represent the exponential decrease of the intensity of the source the time interval between two disintegration was distributed as  $e^{-It}$ , with  $I$  represents the intensity of the source. Another important correction was to assign the real position of the hit to the centre of gravity of the pixel. This is because with the simulation we have precise information about where the particle was detected, while in reality we will only know in which pixel the particle was detected. A further effect to consider is the dependance of the time resolution on the energy deposit  $E_{dep}$  in the sensor, which is proportional to the charge collected. To do so we applied a gaussian smearing to the true signal with a standard deviation parametrised according to an energy dependence as in Equation 4.1:

$$\sigma_t = \sigma_t^0 * \frac{E_{dep}^{MIP}}{E_{dep}} \quad (4.1)$$

Where for  $\sigma_t^0$  we used the value of 106 ps that was measured in [14], and  $E_{dep}^{MIP}$  is the most probable energy-deposit value for minimum ionising particles passing through 100  $\mu\text{m}$  of silicon. Finally the custom software takes into account the geometry of the TT-PET scanner and all the different type of coincidences that we have, to ensure the possibility of an accurate analysis of

our results. To take into account the count losses, the dead time due to the data transfer from the modules to the tower control, and from the latter to the PC, have been taken into account.

The expected TOF resolution was studied analysing the distribution of the TOF between two hits in coincidence, as described in [8]. The full width at the half maximum (FWHM) of this distribution was 80 ps, from this value we obtain a standard deviation of 34 ps. Considering that a coincidence event is triggered by two detector, if we assume that the response of the two detector is the same we can find the time resolution of a single detector simply by dividing the previous value by  $\sqrt{2}$ . The result is that the expected time resolution of a single detector is 24 ps which is coherent with the time resolution goal of 30 ps.

## 4.2 Type of Coincidences

In order to study the sensitivity of the detector we can divide our events based on the  $\gamma$  rays' path before and after entering the scanner. The main difference among the events that we can detect in a PET scanner is based on where the two  $\gamma$  rays came from before reaching the sensor. There are four main different types of events: true, scattered, random and multiple events. Once the particle enters the scanner it can behave in different ways, we can collect these informations and use them to further classify the events on the basis of those differences.

### 4.2.1 True, Random and Scattered Coincidences

As seen above, four main different types of possible coincidences for PET scanners exists: true, scattered, random and multiple (Figure 4.2.1). A true coincidence (Figure 4.2.1A) occurs when the  $\gamma$  rays do not have any interaction while traveling from the annihilation point to the detection point. This

is the type of coincidence that carries the correct information about the annihilation point, that is why we will focus on maximizing the number of true coincidences detected while keeping the other types as low as possible. A random coincidence (Figure 4.2.1C) occurs when two  $\gamma$  rays not produced in the same annihilation are detected within the coincidence time window of the system. We have a scattered coincidence (Figure 4.2.1B) when at least one of the  $\gamma$  rays undergoes to at least a Compton scattering during its path to the detector. Random and Scattered coincidences effect the precision of our reconstruction because they cause a wrong LOR to be assigned to the event.

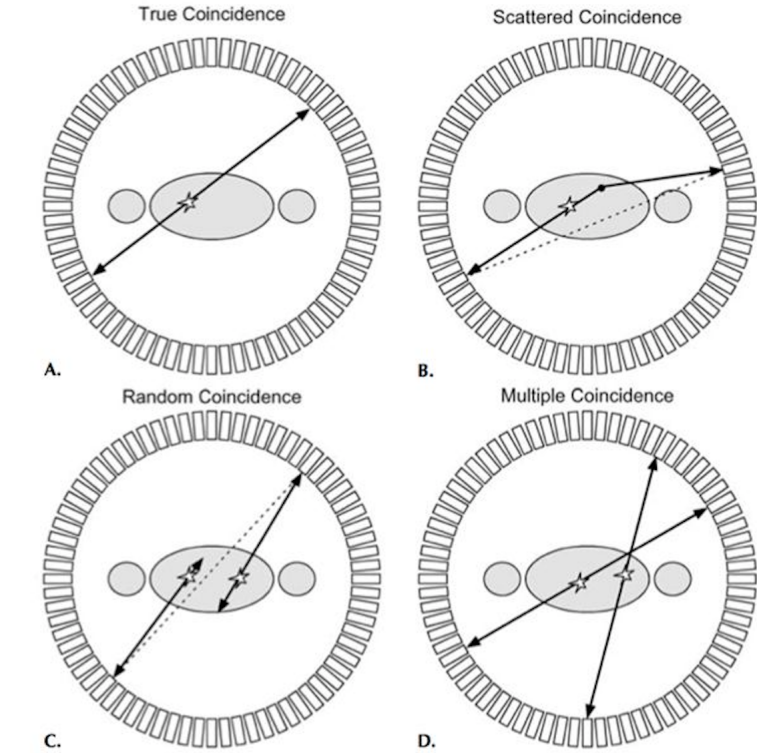


FIGURE 4.1: PET coincidence event types: true, random, scattered and multiple coincidences.

Multiple coincidences events (Figure 4.2.1D) are those coincidences for which more than two  $\gamma$  are detected within the coincidence time window. Since in this situation it is not possible to determine the LOR to which the event should be assigned those type of events will not be considered in our analysis.

In addition it is possible to divide our events in different categories also based on what happens to the incoming  $\gamma$  rays after they enter in the detector. A  $\gamma$  ray, in fact, can interact in different ways with the material in it. Ideally the  $\gamma$  ray will be converted and detected by one of the 60 layers of one of the towers. This case will be considered as a normal event and will have no further classification. However a couple of different cases can happen. The first one is the one in which the charge generated by the converted electron will be collected by more than one sensor, in this case we talk about shared charge events. The second one is when the  $\gamma$  ray, after leaving a signal in a layer is scattered and reaches an outer layer inside the tower, thus generating two signals.

Finally lost coincidence are those events that are registered in the recovery time of the read-out. Since they occur in the dead time of the read-out we also refer to them as dead time coincidences. Those events become significant when the intensity of the incoming radiation increases. We have design the detector to keep this kind of events as low as possible.

#### 4.2.2 Noise Equivalent Count Rate

The noise equivalent count rate (NECR) is used to estimate the number of true counts acquired per second exempt of scattered and random coincidences and contribution from the intrinsic radioactivity of the system. This quantity gives important information about the capability of a detector to have a clear reading of the true events. Noise equivalent count ratio is defined by the following equation:

$$\frac{True^2}{(True + Random + Compton)} \quad (4.2)$$

### 4.3 Time Coincidence Window

It is important to study how the data rates are effected by time coincidence window values because different values of the time coincidence window could change the sensitivity of the detector to lost coincidences. This consideration is also valid for Compton and random events, it is easy to expect that if we set an higher value for the time window we will detect more of this events.

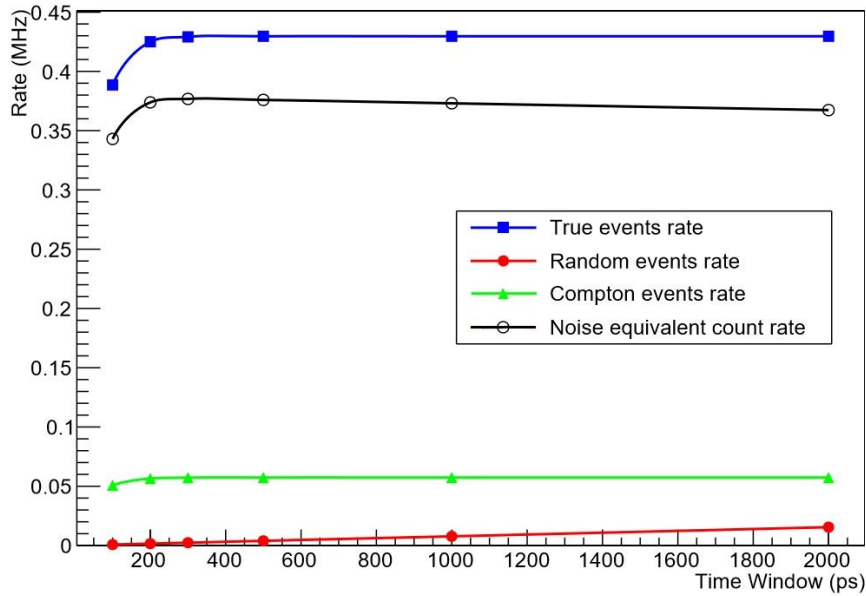


FIGURE 4.2: The plot shows the evolution of True, Random, Compton and NECR events rate for different time window values. If we focus on NECR rate we see a peak round 300 ps, we don't see a deterioration in the rate value after this value. In addition, we see that Compton and Random rates values are low compared to the True events rate, this means that the background noise is low.

The crucial result that we obtain from this study is the value for the time window at which we minimize the losses of true events. This is important because we will use this ideal value for the time window when we will measure the variation of the rates in comparison with the variation of the intensity. The precise purpose of this operation is to find the value of the time window for which we have a drop in the true coincidence rate, so that we

are sure to operate above this value. Since the random events decrease linearly with the time window this step will allow us to minimize the random coincidences detected while avoiding the loss of a significant fraction of true coincidences.

For this simulation we have used a mouse-like phantom made of a solid cylinder of high density polyethylene 50 mm long and 25 mm in diameter, as described in NEMA procedure for a mouse like phantom, but with reduced length to reproduce the exact dimensions of our detector. The radionuclide used is  $^{18}\text{F}$  and is placed in a 3.2 mm cylindrical hole parallel to the central axis at the radiance distance of 10 mm. The intensity of the fluor source is 50 MBq, and the study varying the time window from 50 ps to 2000 ps.

The results of the study are shown in Figure 4.2. For values of the time window above 200 ps the loss of true event is negligible. In addition we see that the rate of Random and Compton events remains low compared to the True events rate even for time windows up to 2000 ps. For the purpose of our intensity rate studies we will not need to use such wide time windows and we will only use time windows of 350, 500 and 1000 ps, sufficiently above the true events drop.

## 4.4 Coincidence rate

As mentioned at the beginning of the chapter the study was developed following the NEMA procedure, [13], that defines the international standards used to assess the performance of small-animal PET systems. Studying how the scanner behaves as a function of the source activity is important both to understand which are the strengths and weaknesses of the detector and to have useful information that can help in the design of the scanner and the data-acquisition system.

For the study of the coincidence rate as a function of the source activity the phantom used was a cylinder of  $^{18}\text{F}$ , 50 mm long with a radius of 1.6 mm. The simulation was repeated for a wide range of source activity, starting from 5 MBq up to 300 MBq. We made this choice to test the scanner response to extreme condition that are far beyond of the operational activities at which the detector will operate.

The condition that we have chosen to define a coincidence event are: a time window,  $\Delta t$ , of 500 ps; line of response (LOR) that intercepts the phantom and an energy deposit in the pixel above 20 KeV for both the hits. With the definition of our constraints for the coincidence events we can now give a definition of the event rates that we studied:

- The *Total* rate represents the total number of coincidence events that are detected by the scanner. We decided to divide this category into two further ones, to take into account also the total rate including lost coincidences. This allowed us to study the intensity level at which the scanner begins to saturate.
- The *Random* events rate shows the coincidence events that are not generated by the same annihilation but are detected within the selected time window.
- The *Compton* events rate shows the coincidence events in which at least one of the  $\gamma$  rays undergoes a Compton scattering during its path to the detector.
- The *True* events rate is defined as the difference between the *Total* rate and the *Random* plus *Compton* rates. Random and Compton rates are generated by different annihilations and will result in a false line of response.



- The *NECR*, or noise equivalent count rate, was already defined in paragraph 4.2.2 as indicated in equation 4.2:

$$\frac{True^2}{(True + Random + Compton)} \quad (4.3)$$

The data acquisition system has an important effect on the performances of the scanner and needed to be taken into account in our simulation. In particular, it effects the count losses, and consequently effects the saturation of the detector.

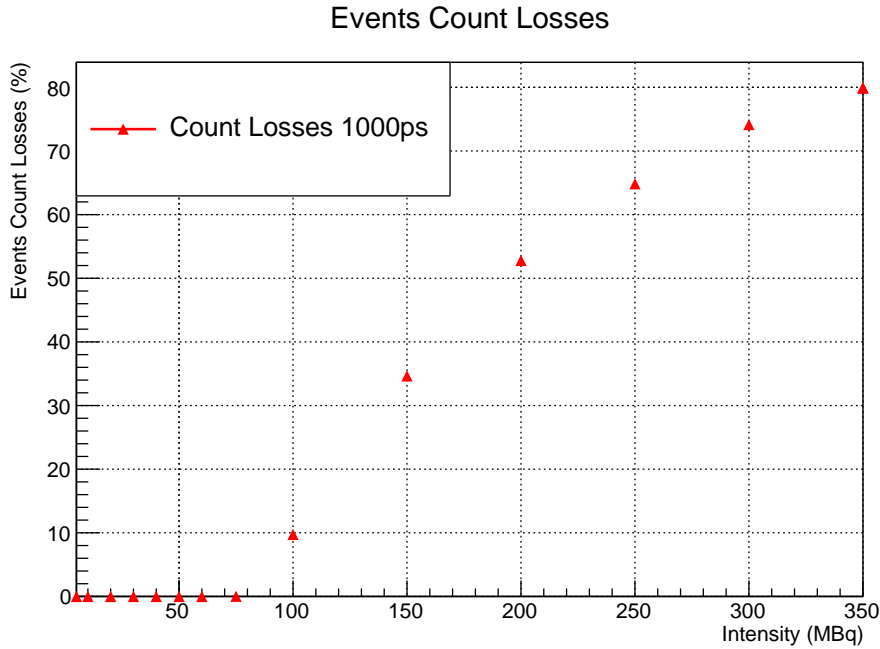


FIGURE 4.3: Simulation of a cylinder 50 mm long, with a radius of 1.6 mm as described in NEMA. Coincidence events occurring during the dead time of the read-out generates count losses, we have estimated to be able to keep those losses under 0.1% even at intensities much higher than the ones at which the TT-PET scanner will operate.

Figure 4.3 shows the expected count losses for the TT-PET detector at different source intensities, we can observe that we have been able to keep the expected lost coincidences at less than 0.1% for incoming intensity up to 75 MBq. It must be pointed out that this is a very good achievement because

this level of intensity is much higher than the one at which the TT-PET scanner should operate. For the simulation we have chosen an high value for the time window, 1000 ps in this case, the reason for this choice is that a larger interval for coincidence selection will result in an higher event rate and consequently in an higher probability of incurring in count losses. We expect the count losses due to dead time coincidences to be even lower for the 500ps time window used in our scanner simulation. To achieve this excellent efficiency in avoiding count losses a fast read-out system was needed, to keep the recovery time as low as possible. From this study some states of buffer both at chip and tower control level have been taken into account in order to maintain the performance optimal. We added respectively 8 states for the chip and 128 for the tower control. In this way, in case of a statistical fluctuation in the rate of detected signals, we are able to store some of those events, and later transfer them to the read-out system. To simulate this effect our custom software had to take into account the dead time of  $2\ \mu\text{s}$ , as well as the dead time to transfer data from the tower control to the board, 40 ns.

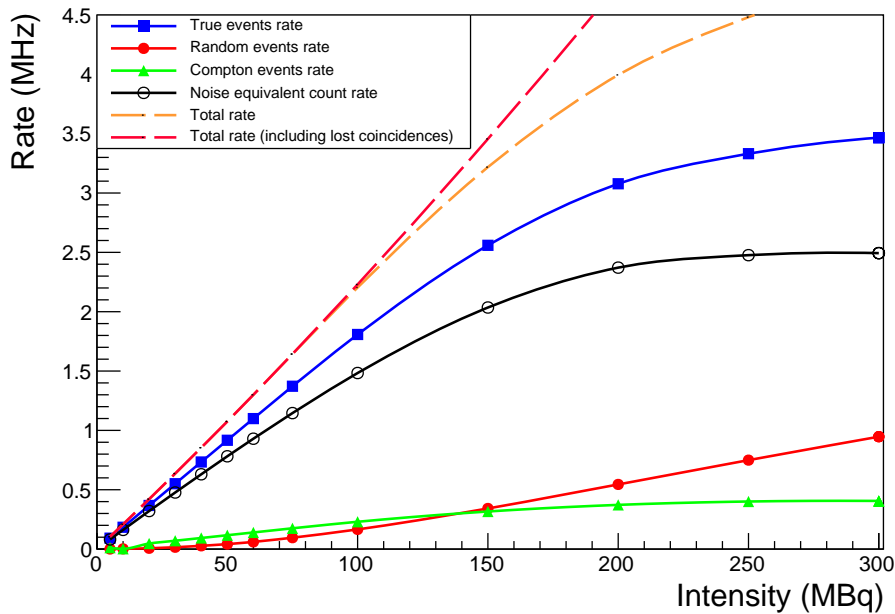


FIGURE 4.4: Coincidence rate as a function of the activity for a cylindric phantom as described by NEMA.

Figure 4.4 shows the results of the simulation of the different rates as a function of the activity for the cylindric phantom and the condition described above. First we look at the *Total* rates, that are represented by the red and orange dotted lines in the plot, we can see that the scanner saturates around 100 MBq, this proves that our configuration is very resilient to count losses even at higher activity levels than those needed. It is important to point out that the Random and Compton rates rise with the intensity but remain small compared to the True rate, especially at low intensity values. This is particularly important because the structure of the TT-PET scanner, with thin silicon detection layer, while being excellent to measure the depth of interaction, does not provide a measurement of the energy loss by the  $\gamma$  ray. For this reason our detector can not distinguish a true coincidence from a Compton one, so having a Compton rate as small as possible, compared to the True rate, is crucial. The results show that the Compton events rate is small and so does not effect significantly the performance of the scanner. Finally, we see that the noise-equivalent count rate saturates at intensities above 200 MBq.

The study was repeated with other two different phantoms. The first of those phantoms was the ideal case of a point-like source placed in the center of the scanner and surrounded by a cylinder of water with length the full length of the scanner and diameter of 3,6 cm. The same conditions used for the previous study for the time window and the dead times of the acquiring system were used. The outcome of the simulation with this phantom is shown in Figure 4.5.

The last phantom that we studied was a spherical source with a radius of 0.3 mm at the center of an acrylic cube with a side of 1 cm. This phantom simulates the case in which only a small part of the animal needs to be scanned, and was used also to study the expected sensitivity as a function of the position along the axial FOV [8].

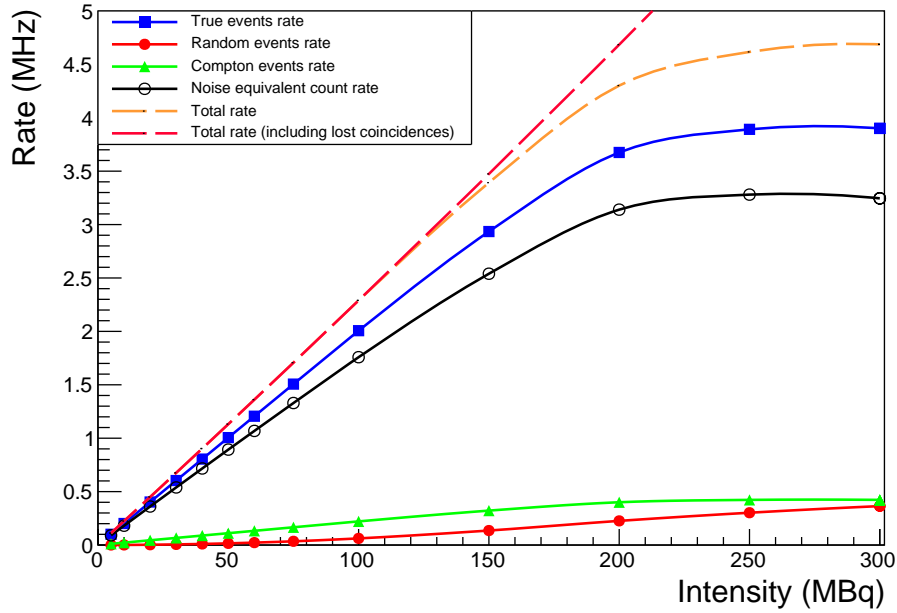


FIGURE 4.5: Coincidence rate as a function of the activity for a point like source in the center of the field of view, surrounded by a cylinder of water with a diameter of 3,6 cm

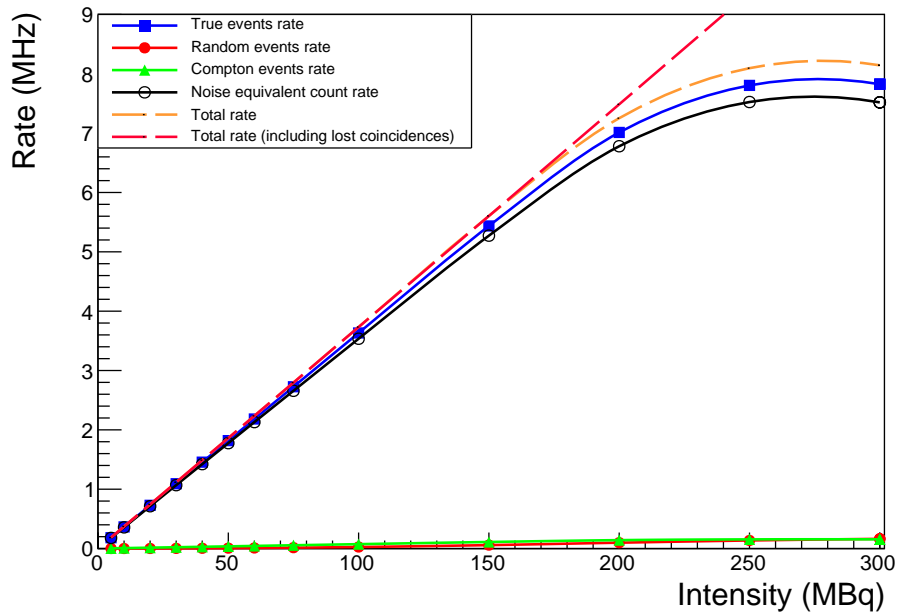


FIGURE 4.6: Coincidence rate as a function of the activity for a small sphere at the center of the field of view.

The results are shown in Figure 4.6. We see that the amount of Random and Compton scattered coincidences is very low and the scanner detects mostly True coincidences. The saturation starts around 200 MBq, well

above the other cases.

#### 4.4.1 Read-out system effect on data rate

We have seen previously in this chapter how a small or big value of the coincidence time window is related to a lower or higher lost coincidence events rate. To complete the study on the lost coincidence rate we also had to consider the effects of the system dead-time. To do so we have compared the results obtained with the cylindrical phantom using different dead times for the data transfer from the chip to the tower and the one from the tower control to the board. In Figure 4.7 are shown the results obtained for a dead time from the tower control to the board of 300 ns, instead of the 40 ns dead time of Figure 4.4. As expected the number of lost coincidence events increases with the increase of the dead time of the read-out system. We see that with this configuration the scanner starts saturating around 75 MBq instead of 100 MBq of the previous configuration, and the NECR has a peak at around 150 MBq while previously the peak was not visible neither at 300 MBq, the maximum simulated intensity.

### 4.5 Scanner Sensitivity

The scanner expected sensitivity was studied with the same spherical phantom used for the last study of the previous paragraph. However for this particular study we have used a 1MBq source and we placed it in 49 position along the z-axis with steps of 1 mm. Figure 4.8 shows the expected sensitivity as a function of the source position for the entire axial FOV. The scanner sensitivity presents a maximum value at 4% for a source at its centre, with a medium sensitivity around 2%.

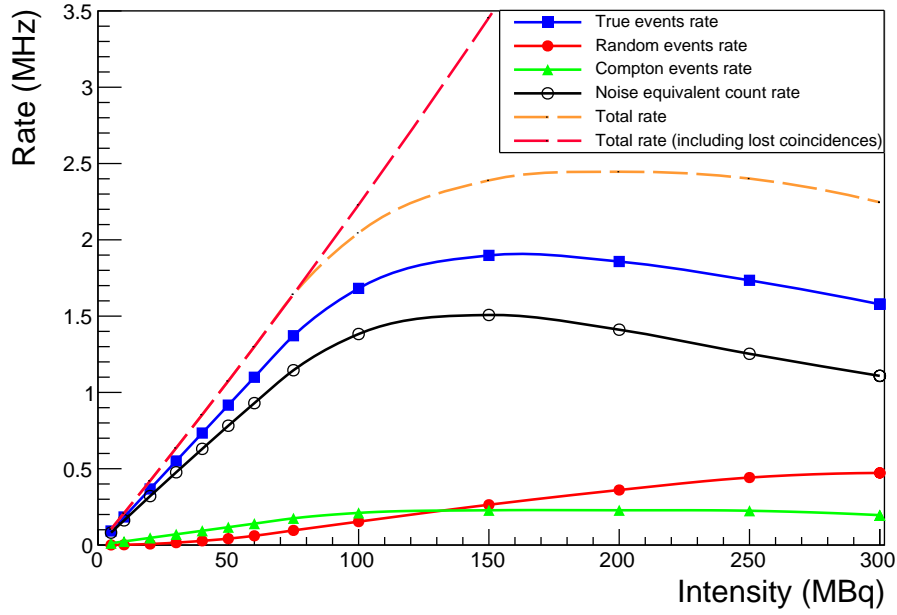


FIGURE 4.7: Coincidence rate as a function of the activity for a cylindric phantom with a dead time to transfer data from the tower control to the board of 300 ns. The scanner is still performing well at operational values of the intensity but it saturates earlier.

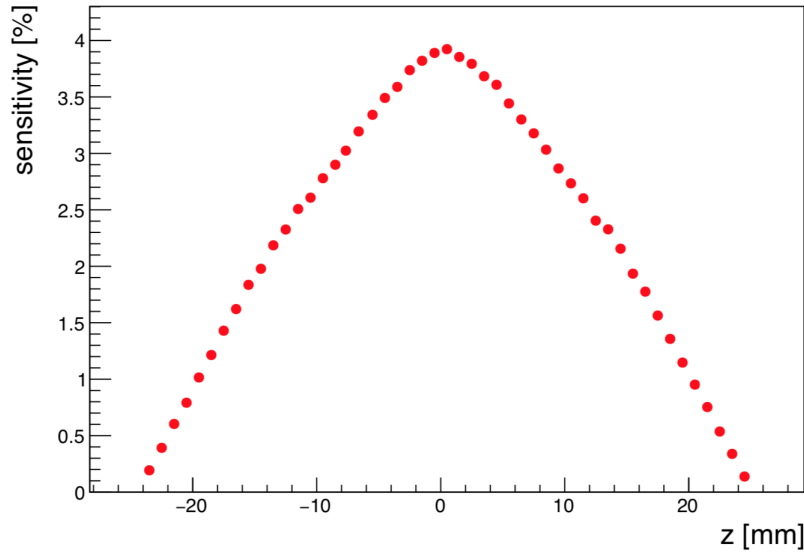


FIGURE 4.8: Expected sensitivity as a function of the position along the axial FOV.

## 4.6 Expected spatial resolution

The spatial resolution of a system represents its ability to distinguish between two points after image reconstruction. To study the spatial resolution of the

TT-PET scanner we have used as phantom the spherical source with 0,3 mm radius described in the previous paragraph. The radionuclide used for this measurement was  $^{22}\text{Na}$ . As requested in NEMA the activity has to be less than that at which either the percent dead-time losses exceed 5% or the random coincidence rate exceeds 5% of the total event rate. Following the procedure we have studied the resolution placing the phantom in 8 different positions. A set of position were at  $z = 0$  in the axial field of view, and 0, 5, 10, 15 mm in the radial coordinate. The second set had the same radial positions but was placed at  $z = 12,5$  mm that is the position that corresponds to a quarter of the axial field of view.

The goal of this measurement is to characterize the widths of the reconstructed image point spread functions (PSF), that describe the response of an imaging system to a point source. For each position the point spread function, was reconstructed using the Customizable and Advanced Software for Tomographic Reconstruction (CASToR) framework [15]. The width of the PSF was estimated measuring the full width at half maximum, FWHM, of the point spread function and also the full width at tenth maximum, FWTM, as a quality measure of the sharpness of a peak. A result compatible with two-dimensional filtered back projection was found already at two iterations. The results of the study are shown in Table 4.1.

<b>z position [mm]</b>	<b>0</b>				<b>12.5</b>			
<b>x position [mm]</b>	<b>0</b>	<b>5</b>	<b>10</b>	<b>15</b>	<b>0</b>	<b>5</b>	<b>10</b>	<b>15</b>
<b>FWHM radial [mm]</b>	0.59	0.57	0.56	0.52	0.65	0.61	0.60	0.56
<b>FWHM tangential [mm]</b>	0.60	0.60	0.67	0.71	0.64	0.65	0.65	0.70
<b>FWHM axial [mm]</b>	0.50	0.49	0.50	0.51	0.45	0.45	0.45	0.45
<b>FWTM radial [mm]</b>	1.8	1.6	1.5	1.4	2.0	1.8	1.7	1.6
<b>FWTM tangential [mm]</b>	1.8	1.7	1.9	2.0	2.0	1.9	1.9	2.0
<b>FWTM axial [mm]</b>	1.2	1.1	1.1	1.1	0.9	1.0	1.0	1.0

TABLE 4.1: Spatial resolution in the transverse FOV calculated for four radial positions: 0, 5, 10, 15 mm from the center of the scanner. The resolution were calculated at the center and at one quarter of the axial FOV.

The values of the FWHM in the different positions within the FOV are below 0.75 mm. The variations in the radial, tangential and axial components are small. As expected, when we move the source in one particular direction we improve the spatial resolution for that component, while slightly decreasing it for the others, this is evident if we compare the radial and tangential values.

The simulation highlights the absence of the typical degradation of the spatial resolution at large values along the radial direction, which is shown in Figure 4.9. This is one of the upsides of the particular structure of the TT-PET scanner, precisely the high granularity due to the 60 detection layers. In fact, while for events close to the center of the axial FOV the sensitivity of a scanner with low granularity is comparable to the sensitivity of a scanner with high granularity, such as our scanner, when we move to the borders of the region of interest the TT-PET scanner, having a better measurement of the depth of interaction (DOI) shows only a small sensitivity degradation. This is a result of the fact that having many layers allow us to have a smaller uncertainty in the reconstruction of the LOR for sources that are not in the center of the operative region.

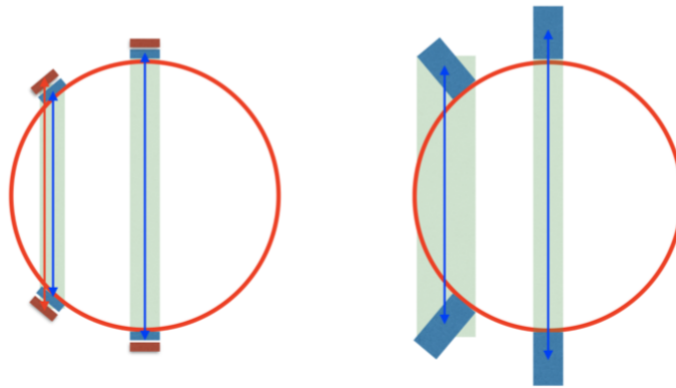


FIGURE 4.9: Schematic representation of the uncertainty in the LOR of sources at the center and at the periphery of a PET scanner. The high DOI granularity of the scanner on the left side of the figure produces better results for sources at the periphery of the scanner.



## Chapter 5

# Image Reconstruction

In the medical imaging field, the interpretation of the underlying biological or pathological processes depends on the precision and the accuracy of the reconstructed images. For this reason tomographic image reconstruction is an essential step for the production of high quality images. In this chapter we will look at how we performed the image reconstruction of a sample Derenzo phantom and we will see the results of adding time of flight information to reconstruct the image, which is one of the main features of the TT-PET scanner. The complete description of all the steps required to go from the events data to the reconstructed image was examined in Chapter 2 and much details on image reconstruction techniques are available in Appendix A. The sum of the all counts recorded along a line of response measures the associated activity, this quantity is called *line integral*. When we combine a full set of line integrals we create a projection profile. The full set of projection data can be displayed in a matrix whose representation is called sinogram. From the sinogram, or the projection profiles, we can reconstruct the image using different techniques like filtered back projection or iterative reconstruction algorithms. Simple back projection is the simplest way to reconstruct an image, some filters are necessary to avoid image blurring, the downside is that the image reconstructed in this way often contain some artifacts. Iterative reconstruction algorithms are computationally more intensive than FBP but allow to include pre- and post-processing data manipulation directly in the

algorithm resulting in a net improvement in the quality of the final reconstructed image.

## 5.1 Derenzo phantom image reconstruction

The Derenzo phantom is one of the most common quality control phantoms for nuclear medicine imaging [16]. The phantom consists of a series of positron emitting rods separated by twice their diameter in a triangular close-packed configuration. Several different rod diameters are typically employed, in this way it is easier to distinguish the diameter at which resolution breakdown occurs.

Since the TT-PET scanner can acquire projection data at oblique angles in the axial direction we can use this information to perform the 3D reconstruction of the image using the single slice re-binning method shown in Appendix A.

### 5.1.1 Reconstruction with filtered back projection

The Derenzo phantom used in our study consists of 40 mm long rods of different diameters: 0.5, 0.7, 1.0, 1.2, 1.5 and 2.0 mm. The rods with the same diameter were disposed in a triangular configuration, the total intensity of the simulated phantom was 50 MBq. The image was reconstructed using a custom software based on the filtered back projection algorithm, the z axis was re-binned in 20 slices of 2 mm according to the single slice re-binning method shown in the Appendix A.

To highlight the importance of adding the information about the time of flight for the image reconstruction process we have compared the reconstructed image obtained using the filtered back projection technique alone to an image obtained adding the time of flight information. In Figure 5.1 is shown the result of the simple image reconstruction. As expected, the high

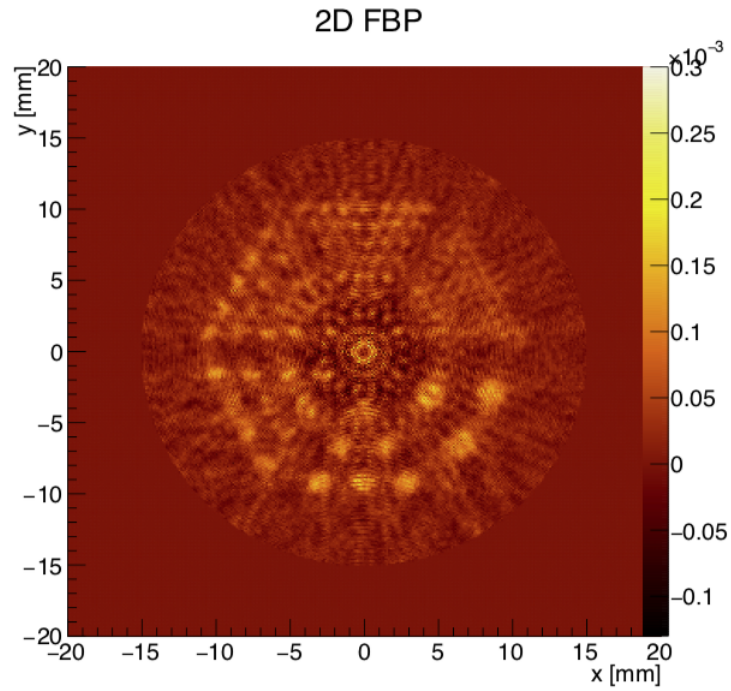


FIGURE 5.1: Image for the Derenzo phantom obtained without TOF information. The rods simulated had diameters of 0.5, 0.7, 1.0, 1.2, 1.5 and 2.0 mm.

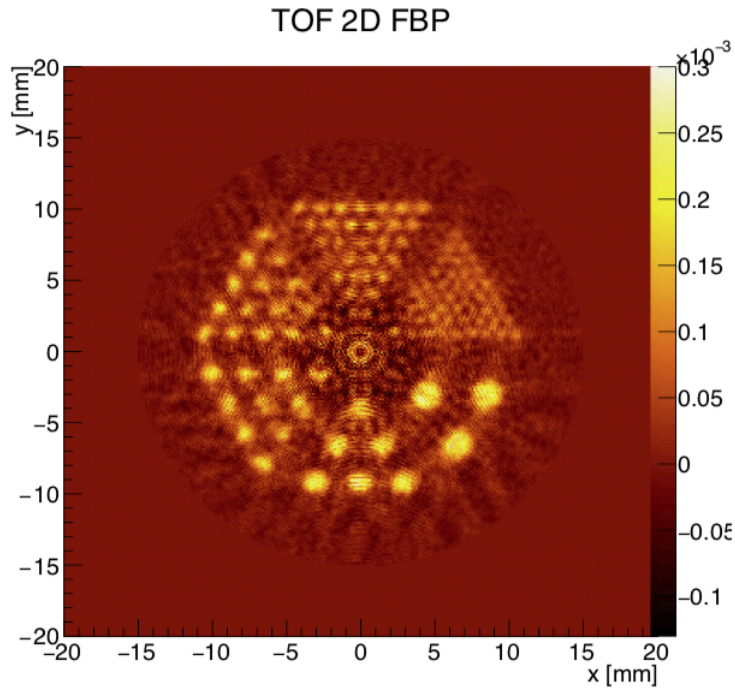


FIGURE 5.2: Image for the Derenzo phantom obtained with TOF information. The rods simulated had diameters of 0.5, 0.7, 1.0, 1.2, 1.5 and 2.0 mm. This reconstructed image is better than the one obtained without TOF and even the 0.5 mm rods can be distinguished.

granularity of the TT-PET scanner allows to resolve the 0.7 mm rods, while the excellent DOI strongly reduces the image degradation of sources at the periphery of the scanner. However this simple reconstruction method generates an artifact at the centre of the scanner, which is expected to disappear when iterative methods will be used. The advantage in using the scanners like the TT-PET scanner for image reconstruction is clear when we look at Figure 5.2. The image represents the same phantom reconstructed adding the TOF information. We can use the very precise measurement of TOF in the back-projection operation, and distribute the count with a normal distribution around the reconstructed annihilation point, we can locate this point using the time difference between the signals. The result is that the signal-to-noise ratio is found to improve significantly and even the 0.5 mm rods can be resolved, although the artifact at the center of the scanner remains in the image.

An alternative reconstruction method to FBP are iterative reconstruction techniques. The advantage with respect to FBP is that it is possible to include the pre- and post-processing data manipulation directly in the algorithm. On the other hand these extra features make these methods computationally more intensive than FBP. The upside in using iterative reconstruction algorithms instead of FBP is the net improvement in the quality of the final reconstructed image.

The iterative reconstruction method is shown in detail in Appendix B.

### 5.1.2 Image Reconstruction with Penalized ML-EM Algorithm

To show power of iterative methods we have reconstructed a Derenzo phantom whose rods had the same diameters of the one used for FBP reconstruction: 2.0 mm, 1.5 mm, 1.2 mm, 1.0 mm, 0.7 mm and 0.5 mm. The method chosen is slightly different [17] from the typical ML-EM algorithm presented

in Appendix B. The new algorithm is build on the EM approach to maximum likelihood reconstruction but it introduces a penalization factor so that unlikely isotope distributions, such as those that are too rough, are disfavoured. We introduce this alternative approach because we have noticed that using the the normal ML-EM algorithm we produce images that have not uniform structures where we expect the phantom distribution to be uniform. Figure 5.3 shows the reconstructed image obtained using the normal ML-EM algorithm without penalization. In the image it is visible how the reconstructed structures are not uniform, especially for larger diameters. These spikes are a characteristic of the ML-EM algorithm that can be fixed with the new algorithm.

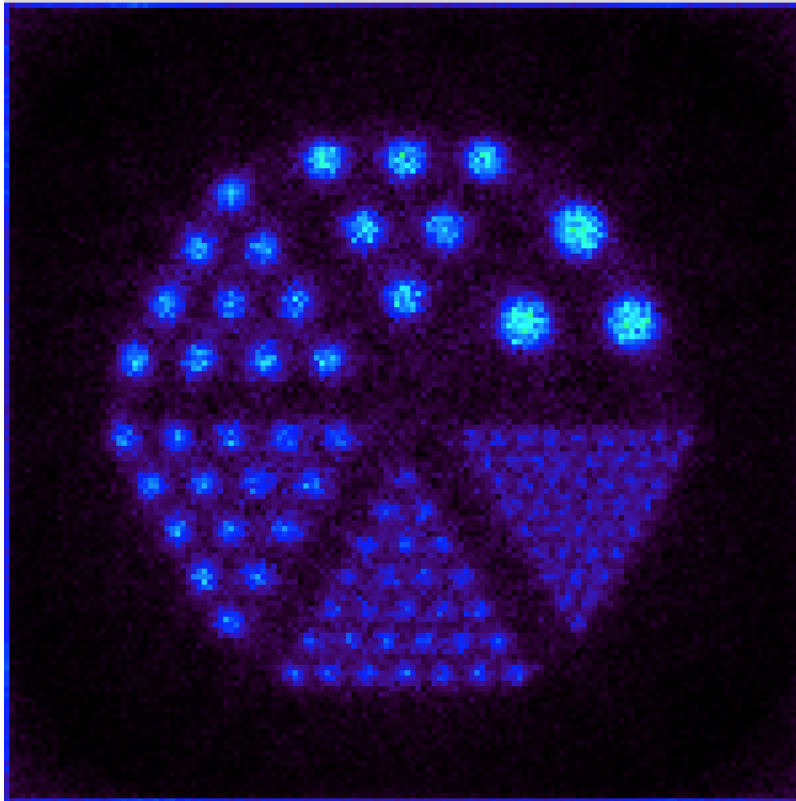


FIGURE 5.3: Image for the Derenzo phantom obtained with 100 iterations of the EM-ML iterative reconstruction algorithm without penalization. The rods simulated had diametres of 0.5, 0.7, 1.0, 1.2, 1.5 and 2.0 mm.

The ML-EM algorithm equation B.2 is then modified, to take into account the new penalization factor, as follows:

$$x_i^{k+1} = \frac{x_i^k}{C_i - \beta \frac{\partial V(x)}{\partial x_i}} \times \sum_j M_{i,j} \frac{p_j}{\sum_l M_{l,j} x_l^k} \quad (5.1)$$

Where the factor  $C_i$  represents the sensitivity map and corresponds to the factor  $\sum_j M_{i,j}$  of equation B.2. The extra factor  $\beta \frac{\partial V(x)}{\partial x_i}$  is the penalization of the algorithm. Beta is an arbitrary parameter that represents the strength of the regularization factor and  $V$  is a potential function that can be expressed as:

$$V(x_i) = \sum_{i,j} w_{ij} \phi(x_i - x_j) \quad (5.2)$$

Where  $w_{ij}$  is a factor that represents the neighbourliness between the pixel that we are evaluating,  $i$ , and the adjacent  $j$ .  $w_{ij}$  value is 1 for adjacent orthogonal pixels and  $\sqrt{1/2}$  diagonal pixels. In our study we have only taken into account adjacent orthogonal pixels, so we have  $w_{ij} = 1$ .  $\phi$  is a function that has to be non-negative, symmetric around 0, and monotonically increasing for positive values of its argument. For our study we have chosen  $\phi = r^2$ . It is important to point-out that when calculating the next iteration  $x_i^{k+1}$  the partial derivative of the potential  $V$  is evaluated at the old value  $x_i^k$ .

For the image reconstruction we have chosen to simulate a 30 minutes exposition of the TT-PET scanner to a 50 MBq source.

Selecting the correct value of beta in equation 5.1 is crucial since a small value would still lead to spikes in the reconstructed image, while larger values will produce an image too uniform making harder to distinguish the structures. After the evaluation of the results for different beta values between 0 and 1000 we have found to have better results with a  $\beta$  values between 50 and 70. Image 5.4 is the result of the reconstruction done using the penalized EM-ML method with  $\beta = 65$ .

When we compare image 5.3 to image 5.4 we see that in the last one the structure of the rods appears to be more uniform and they are much more visible compared to the background. If we look in particular at the 2.0 mm

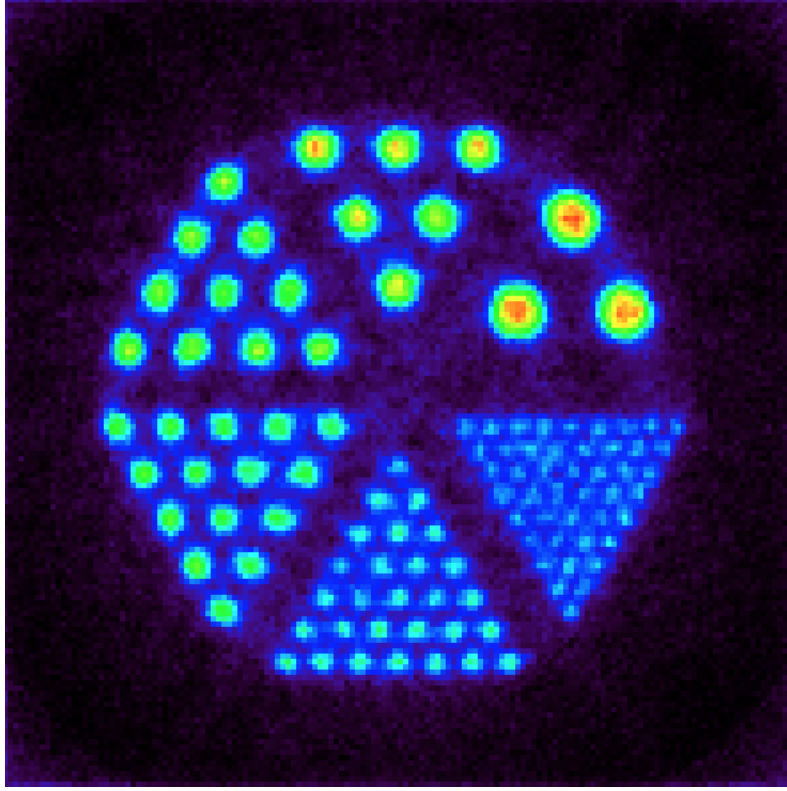


FIGURE 5.4: Image for the Derenzo phantom obtained with 100 iterations of the penalized EM-ML algorithm and  $\beta = 65$ . The rods simulated had diametres of 0.5, 0.7, 1.0, 1.2, 1.5 and 2.0 mm.

rod we can see that the peak (in red) is clearly identified in the middle of the distribution. As for what concerns the final sensitivity we can clearly distinguish the 0.7 mm rods, while the 0.5 mm rods appear slightly blurrier, but are still distinguishable.

The main feature of the TT-PET scanner is ability to get a very precise TOF information therefore is essential to understand which are the advantages of having the possibility to add this information to the reconstruction process. To show these feature we produced an image with the same method and conditions used for image 5.4 but without TOF information, Figure 5.5. While we can obtain the same result with and without the precise TOF information the main difference is that we would need a larger number of iterations, thus a larger computational time, to get to the same quality without TOF. We observe that the reconstruction without TOF generates a poor quality image,

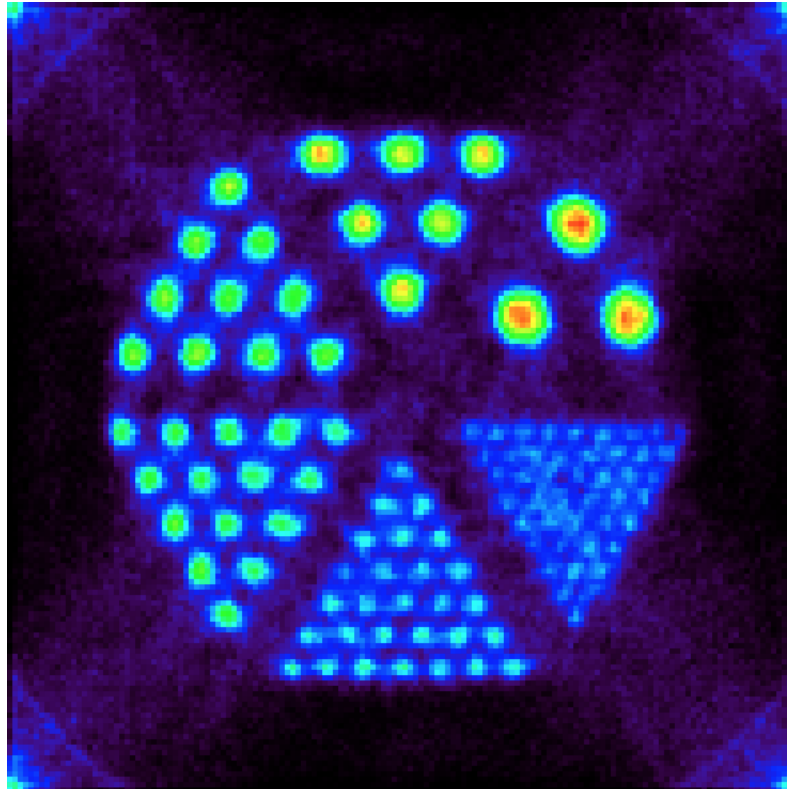


FIGURE 5.5: Image for the Derenzo phantom obtained with 100 iterations of the penalized EM-ML algorithm  $\beta = 65$  but without TOF information. The rods simulated had diameters of 0.5, 0.7, 1.0, 1.2, 1.5 and 2.0 mm.

compared to the one produced with TOF, with evident artifacts in it. This however it is an effect of the normalization map that we have used to produce the images.



## Chapter 6

# Conclusions

The work presented in this thesis is focused on the analysis of the performance of the TT-PET scanner and on the image reconstruction of a sample radioactive source using the very precise time of flight information. The Thin Time-of-Flight PET scanner is a novel compact scanner for small animals developed by the TT-PET group of the University of Geneva and in collaboration with CERN, based on fast silicon detector and aims to a 30 ps time resolution. The final purpose is to use this very precise time information to better reconstruct the position of the source.

### Scanner simulation

In order to achieve the best result it is essential to minimize the count losses and to maximize the ability of the scanner of distinguish the real events from the noise.

Studying the expected count losses for the TT- PET detector at different intensities, we have observed that we are able to keep the expected lost coincidences at less than 0.1% for incoming intensity up to 75 MBq. This is a very good achievement because this level of intensity is much higher than the one at which the TT- PET scanner should operate. To achieve this result we have taken into account the effects of the read-out system dead-time. From our simulation we obtained important feedbacks about the optimal number of buffer states for the chip and the tower control. For a dead time to transfer

data from the chip to the tower of  $2\ \mu\text{s}$ , and a the dead time to transfer data from the tower control to the board of  $40\ \text{ns}$  we have simulated that a 8-state buffer for the chip and 128-state buffer for the tower control were needed.

As a preliminary step to the study of the data rates we have simulated the effects of the time window on the number of count losses and true events. We found out that for values of the time window above  $200\ \text{ps}$  the loss of true event is negligible

Looking at the data rates we expect the TT-PET scanner to saturate around  $100\ \text{MBq}$ , this proves that our configuration is very resilient to count losses even at higher activity levels then those needed. Regarding the Random events rate we have shown that thanks to the high time resolution we are able to keep the time window very small and consequently to reduce the number of these coincidence events. We have also shown that, for a small scanner radius, the incidence of the Compton coincidence events on the quality of the image is negligible. This is particularly important because the structure of the TT-PET scanner, with thin silicon detection layer, even if it is excellent to measure the depth of interaction, does not provide a measurement of the energy loss by the photon and consequently we can not filter out the Compton events. We performed this type of study with three different phantoms: cylindric source, a pointlike source and spheric source.

The expected sensitivity along the axial FOV was also simulated finding a peak value of 4%.

To conclude the study about the expected performance of the TT-PET scanner we estimated the expected spatial resolution for different positions inside the scanner field of view. The FWHM were always below  $0.75\ \text{mm}$  with small variations in the radial, tangential and axial directions. We also found the absence of the typical degradation of the spatial resolution for source far from the center of the FOV in the radial direction. This is an upside of the particular many thin layers structure of the TT-PET scanner.

## Image Reconstruction

The final subject of this thesis has been image reconstruction. We have reconstructed a Derenzo phantom both with filtered back-projection (FBP) and a penalized maximum likelihood expectation maximization algorithm. The Derenzo phantom that we have studied consists of 40 mm long rods of different diameters: 0.5, 0.7, 1.0, 1.2, 1.5 and 2.0 mm.

With both techniques we are able to clearly distinguish all the rods up to the smallest ones. The image obtained with the iterative algorithm are, however, much smoother than those obtained with FBP.

Regarding the iterative reconstruction results it must be point out that we are able to produce a better reconstructed image if we introduce a penalization to the ML-EM algorithm such that unlikely isotope distributions are disfavoured.

To sum up, while potentially one could reach the same results with or without TOF information we have seen that the addition of TOF information to the reconstruction allow us to reduce the computational time needed to produce the image.



## Appendix A

# Image Reconstruction Techniques

The simplest way to reconstruct an image from the acquired profiles is by *simple backprojection*. We consider the case in which we have collected a series of projection profiles from different angles around the source, as shown in Figure A.1. The first step of this technique is to distribute the data from each element in a profile back across the entire image grid. In practice this is done by dividing the counts recorded in a projection profile element uniformly amongst the pixels that fall within its project path. This operation is called *backprojection*. Finally, the backprojections for all profiles are added together and we get an approximation of the distribution of radioactivity of the scanned object.

Mathematically, we can express the backprojection of N profiles using the following formula:

$$f'(x, y) = \frac{1}{N} \sum_{i=1}^N p(x \cos \phi_i + y \sin \phi_i, \phi_i) \quad (\text{A.1})$$

where  $\phi_i$  denotes the  $i^{th}$  projection angle and  $f'(x, y)$  is an approximation of the true radioactivity distribution  $f(x, y)$ . A disadvantage of this procedure is that there are some counts that are projected outside the true location of the source, image B of Figure A.1, as a result the image appears blurred. By increasing the number of projection angles this effect is reduced and the quality of the image improves. We can express the relationship between the

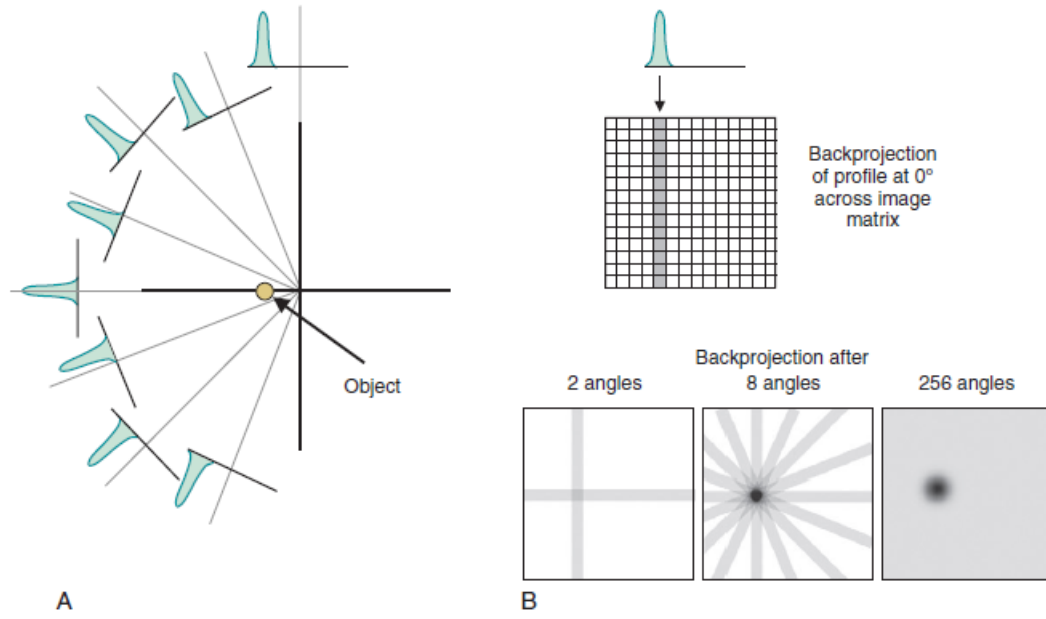


FIGURE A.1: Steps for simple backprojection. A, projection profiles for a point source of radioactivity for different projection angles are acquired. B, backprojection of one intensity profile across the image at the angle corresponding to the profile. This process is repeated for all projection profiles to build up the backprojected image. Image taken from [4].

true image and the reconstructed one using the convolution, indicated by the symbol  $*$ , as:

$$f'(x, y) = f(x, y) * \left( \frac{1}{r} \right) \quad (\text{A.2})$$

For this reason this effect is also known as the  $1/r$  blurring. One approach to avoid the blurring effect is the Fourier transform (FT) reconstruction, also called *direct Fourier transform reconstruction* or *direct FT*. In nuclear medicine imaging, the FT is an alternative method for representing spatially varying data. Instead of representing a 1-D image profile as a spatially varying function,  $f(x)$ , the profile is represented as a summation of sine and cosine functions of different spatial frequencies,  $k$ .

$$F(k) = \mathcal{F}[f(x, y)]$$

the function  $f(x)$  is a representation of the image profile in *image space*, or *object space*, while  $F(k)$  represents the profile in spatial frequencies space, also called *k-space*.

Nuclear medicine CT relies on the *projection slice theorem*, or *Fourier slice theorem*. The above mentioned theorem states that the FT of the projection of a 2-D object along a projection angle  $\phi$ , that can be referred as the FT of a profile  $p(r, \phi)$ , is equal to the value of the FT of the object measured through the origin and along the same angle,  $\phi$ , in k-space:

$$\mathcal{F}[p(r, \phi)] = F(k_r, \phi) \quad (\text{A.3})$$

where  $F(k_r, \phi)$  denotes the value of FT measured at a radial distance  $k_r$  along a line at angle  $\phi$  in k-space.

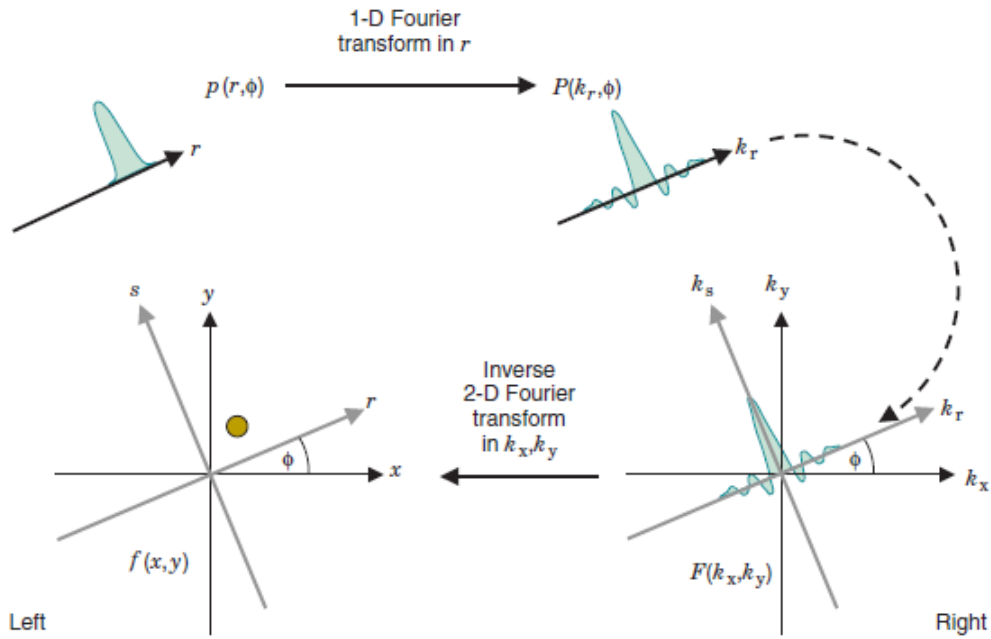


FIGURE A.2: The projection slice theorem. Starting from left we see that  $p(r, \phi)$  is a 1-D profile of the 2-D object  $f(x, y)$  at projection angle  $\phi$ . The theorem states that the 1-D Fourier transform of this projection profile is equal to the values of the 2-D Fourier transform of the object,  $F(k_x, k_y)$ , along a line through the origin of k-space at the same angle  $\phi$ . image taken from [4].

## A.1 Filtered Backprojection

Another way to eliminate the  $1/r$  blurring is the *filtered backprojection* (FBP). FBP uses the projection slice theorem in combination with backprojection. we can divide this procedure in different steps as follows:

1. Acquire projection profiles in object space at  $n$  projection angles,  $\phi_i$ ,  $i = 1, 2, \dots, N$ .
2. Compute the 1-D FT of each profile.
3. Apply a “ramp filter” to each k-space profile, that means multiplying each projection FT by  $|k_r|$ , the absolute value of the radial k-space coordinate at each point in the FT. In this way we get a modified FT for each projection:

$$P'(k_r, \phi) = |k_r| P(k_r, \phi) \quad (\text{A.4})$$

where  $P(k_r, \phi)$  is the unfiltered FT.

4. Compute the inverse FT of each filtered FT profile to obtain a modified projection profile.

$$p'(k_r, \phi) = \mathcal{F} [P'(k_r, \phi)] = \mathcal{F} [|k_r| P(k_r, \phi)] \quad (\text{A.5})$$

5. Do the backprojection using the filtered profiles:

$$f(x, y) = \frac{1}{N} \sum_{i=1}^N p'(x \cos \phi_i + y \sin \phi_i, \phi_i) \quad (\text{A.6})$$

Step 5 is the same as in simple backprojection, but with filtered profiles. However, unlike equation A.1, in which  $f'(x, y)$  is just an approximation of the true distribution of radioactivity, with FBP, when using noise-free data, we get the exact value of the true distribution  $f(x, y)$ . The effect of the ramp filter is to enhance high spatial frequencies and to suppress low ones; the



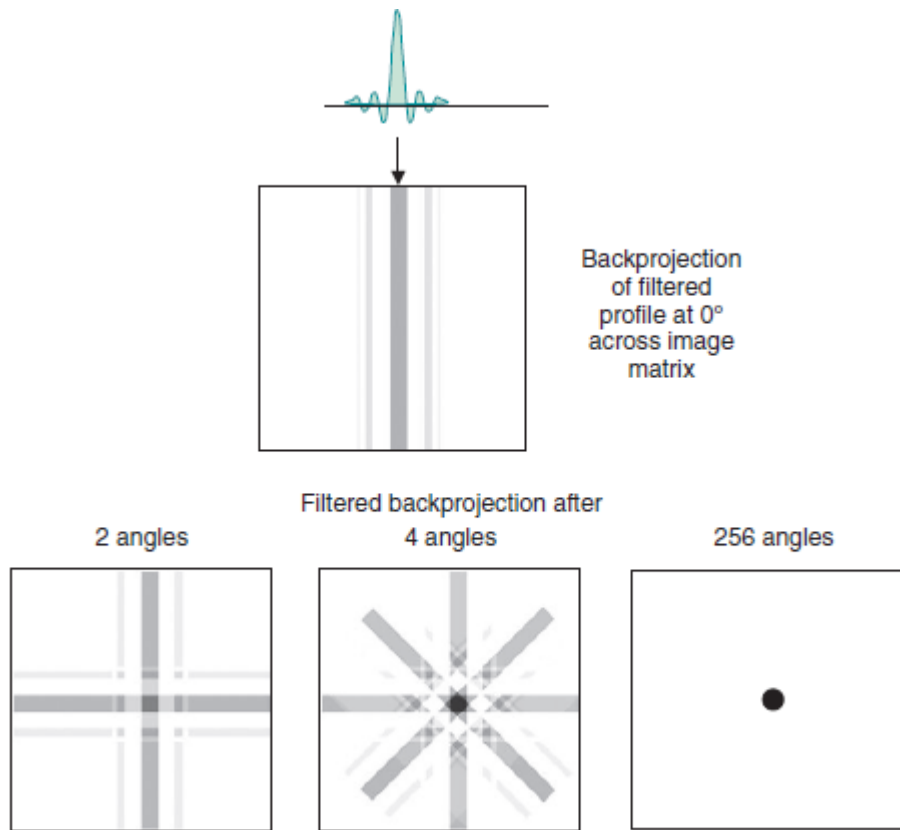


FIGURE A.3: Different steps of filtered backprojection. Image taken from [4].

result of this technique is to eliminate the blurring effect. As a counter effect amplification of high spatial frequencies leads to amplification of high-frequencies noise and so to a worst signal-to-noise ratio. It is, however, possible to minimize this effect choosing appropriate ramp filters.

Using FBP has also some drawbacks. Indeed, this technique is susceptible to major artifacts if data are measured incompletely or datasets have poor statistics or random noise spikes. Moreover this type of algorithm doesn't take into account several physical aspects of the imaging system, this require additional pre or post-processing.

## A.2 3D Reconstruction

To perform the 3D reconstruction we have to take into account the projection data at oblique angles in the axial direction. To incorporate these additional projection angles it is a common approach in image reconstruction to “re-bin”, such that each oblique projection ray is placed within the projection data for a particular non-oblique slice. The most simple method to accomplish this is to assign each ray to its average position along the axial direction. Thus an oblique projection-ray between a detector at location  $a$  and a detector at location  $b$  would be positioned as if it were a projection from a directly opposed pair located halfway between them, i.e., at location  $(a + b)/2$ , Figure A.4 . Processing of all the projection rays in this manner results in a series of sinograms of parallel-ray projections, each corresponding to different axial locations through the object. Each sinogram can then be reconstructed using FBP or iterative algorithms. This method is known as single slice re-binning.

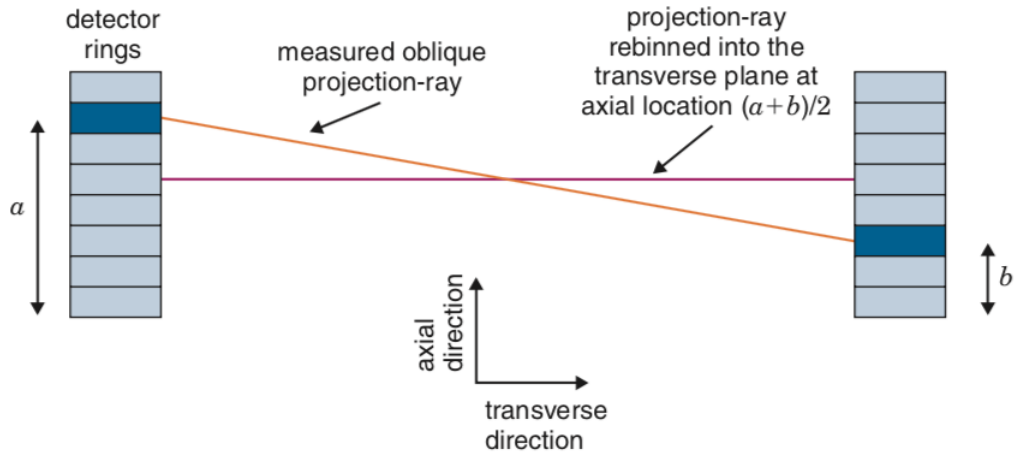


FIGURE A.4: Example of single-slice re-binning in which an oblique projection-ray between the detector pair  $a$  and  $b$  is “re-assigned” to the projection data for the non-oblique slice corresponding to a transverse detector pair at axial location  $(a+b)/2$ .  
Image taken from [4].

## Appendix B

# Iterative Reconstruction

## Algorithms

An alternative reconstruction method to FBP are iterative reconstruction techniques. The advantage in respect to FBP is that it is possible to include the pre- and post-processing data manipulation directly in the algorithm. On the other hand these extra features make these methods computationally more intensive than FBP. Figure B shows the basic steps needed by iterative reconstruction algorithms to reconstruct the true image  $f(x, y)$ . It starts with an initial and very simple image, then the projections that would have been measured for that specific image are computed using *forward projection*. This process consists in summing up the intensities along the potential ray paths for all projections through estimated image. The sinogram generated from estimated image then is compared with the actually recorded sinogram. The difference between the estimated and actual sinogram is used to modify the estimated image to have better agreement. This process is repeated until the difference between the forward-projected sinograms for the estimated image and the actually recorded sinogram falls below some specific level.

Iterative reconstruction algorithms can be divided in two basic components:

1. The method for comparing the estimated and actual profiles. This is

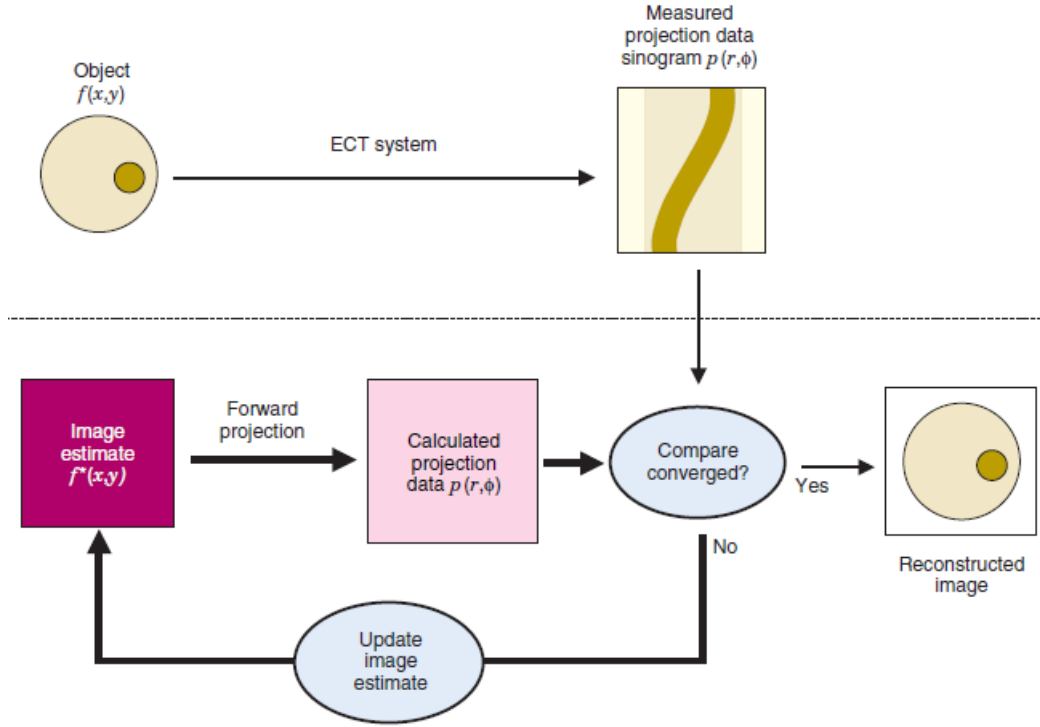


FIGURE B.1: Iterative reconstruction main steps. Image taken from [4].

performed by the *cost function*, which measures the difference between the profiles generated by forward projections through the estimated image and the profiles recorded from the scanned object.

2. The method by which the image is updated based on comparison. This is performed by the *search* or *update function*, which uses the output of the cost function to update the estimated image.

We have seen that iterative algorithms require several iterations to converge to an acceptable image, since each iteration is equivalent to a backprojection procedure it is clear why these type of reconstruction methods are computationally much more demanding than FBP. Moreover iterative algorithms can incorporate factors regarding the specific characteristics of the detector system, this requires further computational power for it to work. Considered the more intensive computational requirements the gain in using iterative reconstruction algorithms instead of FBP is the net improvement in the quality of

the final reconstructed image.

### B.0.1 Expectation-Maximization Algorithm

An example of an iterative reconstruction algorithm is the *expectation maximization* (EM) algorithm. This technique incorporates statistical considerations to compute the “most likely”, or *maximum likelihood* (ML), source distribution that would have created the observed projection data. For these reasons this algorithm is also called the *ML-EM method*. In practice, the algorithm assigns greater weight to high-count elements of a profile and less weight to low-count regions, while backprojection algorithms assign an uniform statistical weighting to all element of a profile.

The reconstruction process goes as follows. First it is calculated the measured activity in the  $j^{th}$  projection element,  $p_j$ , as;

$$p_j = \sum_i M_{i,j} x_i \quad (\text{B.1})$$

where  $x_i$  is the activity in the  $i^{th}$  pixel in the image and  $M_{i,j}$  is the probability that radiation emitted from  $i^{th}$  pixel will be detected in the  $j^{th}$  projection element. Since the  $i$  and  $j$  indices each apply to the full set of the subscripted quantities the matrix  $M$  turns to be very large even in simple cases. This approach provides a potentially more accurate model for relating projection profiles to the underlying source distribution than simple forward projection. The probability matrix  $M$  can be determined by calculations, simulations, or a combination of both.

The equation for computing the estimated activity value  $x$  of pixel  $i$  in the  $(k + 1)^{th}$  iteration of the EM algorithm is:

$$x_i^{k+1} = \frac{x_i^k}{\sum_j M_{i,j}} \times \sum_j M_{i,j} \frac{p_j}{\sum_l M_{l,j} x_l^k} \quad (\text{B.2})$$

Where  $k$  refers to the immediately preceding  $k^{th}$  iteration. The term at the denominator on the right hand side of equation B.2 represents a summation over all image pixels. This term must be evaluated before the summation over the  $j$  projection elements can be computed.

Considering the fact that equation B.2 represents only a single-slice version of the algorithm it is easy to comprehend that one could need a quite high computational power to use this technique. Nevertheless the ML-EM algorithm can produce high-quality images with good quantitative accuracy.

# Bibliography

1. Stewart, B. & Wild, C. World Cancer Report 2014. *International Agency for Research on Cancer, WHO* . Available from: <http://publichealthwell.ie/node/725845> [Accessed: 3rd March 2019] . (2014).
2. Wahl, R. L. *Principles and practice of positron emission tomography* (Lippincott Williams & Wilkins, 2002).
3. Kapoor, V., McCook, B. M. & Torok, F. S. An introduction to PET-CT imaging. *Radiographics* **24**, 523–543 (2004).
4. Cherry, S. R., Sorenson, J. A. & Phelps, M. E. *Physics in nuclear medicine* (Elsevier Health Sciences, 2012).
5. <https://atlas.cern>
6. Vandenberghe, S., Mikhaylova, E., D’Hoe, E., Mollet, P. & Karp, J. S. Recent developments in time-of-flight PET. *EJNMMI Physics* **3**, 3. ISSN: 2197-7364 (2016).
7. Oct 2018. <https://www.mediso.com/products.php?fid=2,11-pid=84>.
8. Ripicini, E. *et al.* Expected performance of the TT-PET scanner. *arXiv preprint arXiv:1811.12381* (2018).
9. Moses, W. W. Fundamental limits of spatial resolution in PET. *Nuclear Instruments and Methods in Physics Research Section A: Accelerators, Spectrometers, Detectors and Associated Equipment* **648**, S236–S240 (2011).
10. Paolozzi, L. *et al.* Characterization of the demonstrator of the fast silicon monolithic ASIC for the TT-PET project. *Journal of Instrumentation* **14**, P02009 (2019).

11. Bandi, Y *et al.* The TT-PET Data Acquisition and Trigger System. *arXiv preprint arXiv:1812.03958* (2018).
12. <http://geant4.web.cern.ch/geant4/>
13. 4-2008, N. N. Performance Measurement of Small Animal Positron Emission Tomographs (PETs).
14. Benoit, M. *et al.* 100 ps time resolution with thin silicon pixel detectors and a SiGe HBT amplifier. *Journal of Instrumentation* **11**, P03011 (2016).
15. Merlin, T. *et al.* CASToR: a generic data organization and processing code framework for multi-modal and multi-dimensional tomographic reconstruction. *Physics in Medicine & Biology* **63**, 185005 (2018).
16. Derenzo, S., Budinger, T., Cahoon, J., Huesman, R. & Jackson, H. High resolution computed tomography of positron emitters. *IEEE Transactions on Nuclear Science* **24**, 544–558 (1977).
17. Green, P. J. Bayesian reconstructions from emission tomography data using a modified EM algorithm. *IEEE transactions on medical imaging* **9**, 84–93 (1990).